The Joule Heating Effect of High-T_c Superconducor $Bi_2Sr_2CaCu_2O_{8+\delta}$ THz Emitting Devices on the Emitting Character

Chiharu Watanabe

January 2017

The Joule Heating Effect of High-T_c Superconducor $Bi_2Sr_2CaCu_2O_{8+\delta}$ THz Emitting Devices on the Emitting Character

Chiharu Watanabe

Doctoral Program in Engineering

Submitted to the Graduate School of Pure and Applied Sciences in Partial Fulfillment of the Requirements for the Degree of Doctor of Philosophy in Engineering

at the University of Tsukuba

Abstract

Since high-T_c superconductor $Bi_2Sr_2CaCu_2O_{8+\delta}$ (Bi2212) single crystals inherently contain intrinsic Josephson junctions (IJJs) within them, it is expected that the stable, coherent and strong THz radiation may be generated from the mesa structure by simply applying a dc voltage to it. This THz radiation was actually discovered for the first time in 2007 in Kadowaki group in the University of Tsukuba in collaboration with Dr.Wai K. Kwok and Dr.Ulrich Welp in the group of Argonne National Laboratory. The most interesting point of this superconducting based THz radiation lies in the emission mechanism that is entirely different from the conventional ones: one is based on the semiconducting or electron tube electronics technology, which can generate the electromagnetic waves in radio waves, short waves, microwaves up to a few hundreds of GHz while electromagnetic waves in the optical frequency, infrared and down to far infrared region can be generated by the energy level transition crossing the forbidden band or optical level transition. On the contrary to these conventional mechanisms, the THz radiation discovered in the high-T_c Bi2212 IJJ systems has an entirely different radiation mechanism, which comes from the ac-Josephson effect and the synchronized oscillation of many series-connected IJJs along the c-axis. It is also known that the cavity resonance effect works very efficiently for a particular shapes of the mesa. The THz emission obtained from IJJ mesa structures is coherent and the electromagnetic waves are similar to the optical lasers, so that there will be many applications both for the basic sciences and practical applications. In particular, as for the most of the applications it is necessary to have higher power radiation intensity, which is desired to be at least $\sim$1 mW. The simplest way to do so may be to increase the number of Josephson junctions involved in the THz emission in the mesa device. However, in practice, thicker mesas containing more IJJs, generate more Joule heating, resulting in a huge local temperature increase in the mesa very inhomogeneously. Often the temperature of a local region well exceeds the critical temperature, T_c, of the superconductor, so it is known as a "hot spot". This peculiar phenomenon has been intensively studied in this thesis in close relation with the THz emission phenomena by directly measuring the local mesa temperature, $T(r)$, using the photoluminescence technique, where SiC micro-crystals were uniformly coated on the surface of the mesa, and they work as a local thermometer during simultaneous spectroscopical investigations of the THz radiation by the FT-IR spectrometer. As a result, we successfully observed the hot-spot thermal images in the higher current bias and the lower bath temperature ($T_b \lesssim 50$ K) region of the current voltage characteristics (IVCs). In addition, we found many interesting phenomena associated with the hot spot at various positions of the IVCs in relation to the emission intensity and the frequency. Such rich phenomena observed in the course of my Ph.D. study have been published in several scientific journal articles as listed at the end of this thesis and will be

summarized here in detail. From the accumulated experimental facts in the course of study, we draw several useful conclusions regarding how to control the hot spot in order to increase the emission power and to extend the emission frequency to higher values, both of which are critically important for practical applications.

Index

All of the figures represented in this thesis are officially admitted by the journals.

Part I

Introduction

1 THz waves: general features and its applications

The electromagnetic (EM) waves with frequency lying between those of visible light and microwaves in frequencies, *i.e.*, 0.3 $\sim$ 3.0 THz (1 THz = 10^{12} c/s), are called terahertz (THz) waves and have many interesting characteristic features. For example, they have both properties of optical light and EM waves; a large permeability to insulating materials such as paper, wood, cloth, plastics, *etc.*, and a strong reflectivity from most metals, *etc.* Furthermore, as shown in Fig. 1, we find that their frequency range overlaps that of the oscillation and relaxation time scales of molecules, lattice vibrations, and of other excitations in gases, liquids and solids. Because of such special characteristics, various THz applications have attracted much attention in a wide variety of research and application fields including not only basic physical and chemical studies of atoms and molecules but also studies of polymer, large molecular compounds, bio-materials, medicine, pharmaceuticals, and analyses of diagnoses of diseases at molecular level, *etc.* [1, 2]. However, in the THz frequency region especially centered at about 1 THz, simple, compact and sensitive THz emitters and detectors have not been available so far. This region is called the "THz gap"[3]. But the recent rapid development of THz devices has been remarkable and the THz gap is now quickly being filled up. The presently promissing candidates of THz emitting devices are summarized below.

1. Quantum Cascade Laser (QCL): It is a semiconductor laser device based on the artificial superlattice structure with a long period and can emit the mid- to far-infrared EM waves demonstrated first by Jerome Faist and others [4]. It has the advantages of being compact, relatively inexpensive, high efficiency, and strong power (1 $\sim$ 100 mW) at a fixed frequency. The oscillation mechanism is based on the intersubband transitions in a repeated stack of multiple quantum well heterostructures. Therefore, the multiple stimulated emission can be induced. Since its emission frequency is not determined by the material's energy band gap but primarily by the thickness of the quantum well, the emission frequency can be chosen freely. However, the emission frequency is also determined by the energy difference between quantum wells, therefore, it is fixed and untunable, and is limited in temperature below $T_{\max} \sim \hbar\omega/k_{\mathrm{B}}$, where $\hbar$ is the Planck constant divided by 2π, $\omega = 2\pi f$, which is the angular frequency of the EM waves, and k_{B} is the Boltzman constant. Therefore, in order to generate EM waves at 1 THz, this QCL has to be cooled down at least to liquid nitrogen temperature.
2. Resonant Tunneling Diode (RTD): It is also a semiconductor device and is based on

quantum resonance tunneling effect predicted by R. Tsu and R. Esaki theoretically [5]. Since RTDs show negative differential resistance, it works as an EM wave emitter by connecting to an external resonator [6]. The biggest advantage is that it can be operated at room temperature. The maximum emission intensity is 0.61 mW at 0.62 THz and the maximum frequency is 1.92 THz so far. Furthermore, there was a report that the emitted radiation from 4 RTDs is tunable from 580 $\sim$ 900 GHz when the RTDs are connected to varactor diodes.

In parallel to the above mentioned rapid development in semiconducting devices, in June, 2007, the Kadowaki group at the University of Tsukuba, Japan, in collaboration with the group of Dr.Wai Kwok and Dr.Ulrich Welp at Argonne National Laboratory in the USA, discovered the new THz emission from a compact mesa structure fabricated from high-T_c superconductor $Bi_2Sr_2CaCu_2O_{8+\delta}$ (Bi2212) single crystals [7]. It was reviewed later that the fundamental mechanism of THz radiation from the high-T_c superconducting mesa structure is nothing but the synchronized oscillation of the superconducting phase of the order parameter through many stacked intrinsic Josephson junctions along the c-axis of the Bi2212 compound. This synchronized phase dynamics is driven by the ac-Josephson effect described by the equation, $f = 2ev/h$, where f is the frequency of the oscillating supercurrent generated by the voltage, v,

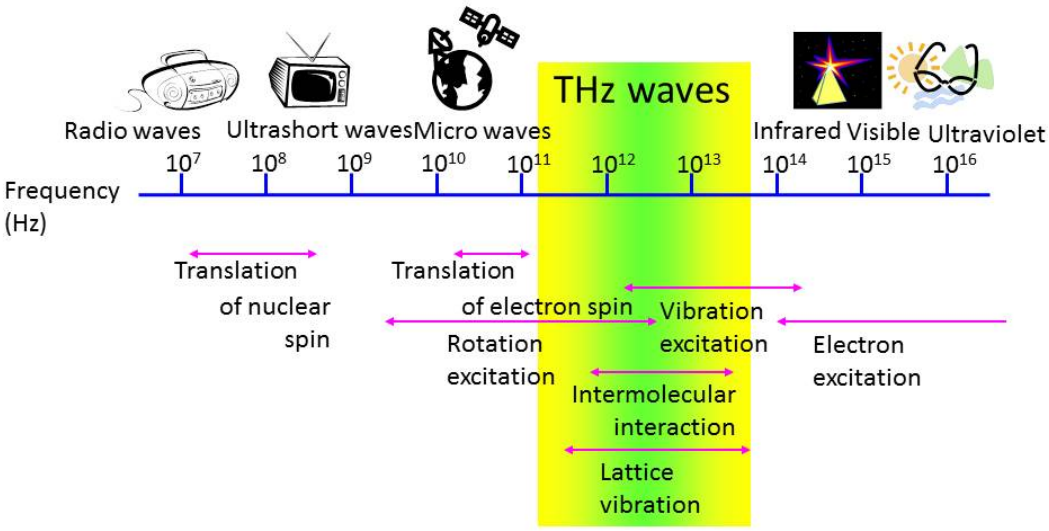

Fig. 1 The vibration spectrum *vs.* frequency of electromagnetic waves (EMs). The electromagnetic waves in 0.3 $\sim$ 3 THz are described as THz waves where there are many energy transfer spectra of molecular rotating excitation. In addition, rotational and vibrational energy levels and the intermolecular interaction energy of macromolecules *etc.* lie in the THz frequency region.

induced at an individual intrinsic Josephson junction, e represents the elementary charge and h is Planck's constant in the non-linear quasiparticle state in the IV (Current-Voltage) curve due to the dc-Josephson effect. In an actual device, the geometrical shape of the device is naturally involved in the radiation and it provides a resonance with an emission frequency and works as a cavity, which can enhance the emission intensity significantly when the geometrical resonance frequency matches the ac-Josephson frequency. The quality factor Q-value of the cavity in the actual mesa devices seems not to be so high, but is an order of ~ 100. Since the radiation is rather strong, coherent, stable and tunable, it may be one of the best candidates of the THz emitting devices to fill in the THz gap. Therefore, we have been motivated to study this sort of devices for improving the emission intensity and expanding the emission frequency range to be useful for THz applications.

2 Josephson junctions

2.1 Josephson effect

In 1962, Brian D. Josephson predicted that when two superconductors are separated by a thin insulating barrier (called a Josephson junction), it may be possible for Cooper pairs to tunnel together through the barrier without a potential difference (quantum mechanical tunneling phenomenon) [8]. Soon after that, Anderson and Rowell actually observed the corresponding phenomenon of Josephson's prediction that a dc-tunneling current at near zero voltage in very thin tin-oxide barriers between superconducting tin and lead electrodes in 1963 [9].

Here, we introduce first the dc-Josephson effect. The concept is that when a Josephson junction is biased by current source less than a certain critical current, no voltage develops between the electrodes on opposite sides at the junction of the junction but the current flows through the barrier by Cooper pair tunneling at zero applied voltage.

The Josephson effect consists of two parts: one is the dc-Josephson effect, which is described by $J = J_{\mathrm{c}}\sin\phi$, where J_{c} is the dc critical current density flowing between two superconductors, and ϕ is the phase difference between them. The other one is the ac-Josephson effect, which can be written as $f = 2ev/h$ where e is the elementary charge, h the Planck constant and v the voltage induced between the two superconductors.

These effects can be described as follows: Firstly, we describe the pair wave functions in the two superconductors separated by the barrier. When the separation between the two superconductors is large enough, each of them is separately described by a macroscopic wave function

$$\psi_k = |\psi_k(r)|e^{i\theta_k(r)}, \tag{1}$$

where $|\psi_k|$ is the amplitude of the wave function representing the pair density, θ_k is the phase of the electron pairs, and $k = 1, 2$ are the indices representing superconductors "1" and "2". In such a case, the phases of two wave functions are independent and unrelated. On the other hand, when the separation between them becomes smaller enough, the wave functions penetrate the barrier from both sides and become coupled. When the coupling energy exceeds the thermal fluctuation energy, the Cooper pairs can flow through the barrier without energy loss. According to Feynman, this situation can be described as follows [10]. The time evolution of the two wave functions which are coupled to each other can be described by

$$i\hbar\frac{\partial\psi_1}{\partial t} = U_1\psi_1 + K\psi_2 \tag{2.1}$$

and

$$i\hbar\frac{\partial\psi_2}{\partial t} = U_2\psi_2 + K\psi_1. \tag{2.2}$$

The U_1 and U_2 are the energies of the wave functions (ψ_1 and ψ_2) of superconductor = "1" and superconductor "2" as shown in Fig. 2 and K is the coupling constant describing the mixing of the wave functions. We suppose that there is a voltage difference ($e^*(V_2-V_1) = e^*V$) between the two superconductors, which can be expressed as $U_2 - U_1 = e^*V$. For simplicity, we define $U_1 + U_2 = 0$ and equation (2) becomes

$$i\hbar\frac{\partial\psi_1}{\partial t} = -\frac{e^*V}{2}\psi_1 + K\psi_2 \tag{3.1}$$

and

$$i\hbar\frac{\partial\psi_2}{\partial t} = \frac{e^*V}{2}\psi_2 + K\psi_1. \tag{3.2}$$

For convenience, the wave function ψ_k (k =1 or 2) can be expressed in terms of the density of Cooper pairs n_k as,

$$\psi_k = (n_k)^{1/2}e^{i\theta_k(r)}, \tag{4}$$

where r is the scalar function of the position. By substituting equation (4) into (3.1) and (3.2), separating the real and imaginary parts and assuming $\phi = \theta_2 - \theta_1$, we come to the following

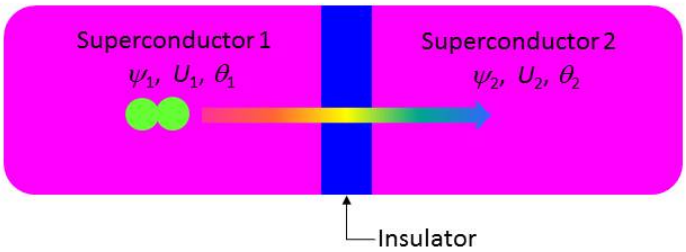

Fig. 2 The schematic picture of a Josephson junction. The Cooper pairs flow through the insulating barrier without energy loss when two superconductors ("1" and "2") are separated by a sufficiently thin insulating barrier.

equations:

$$\frac{\partial n_1}{\partial t} = \frac{2}{\hbar} K (n_1 n_2)^{1/2} \sin\phi, \tag{5}$$

$$\frac{\partial n_2}{\partial t} = -\frac{2}{\hbar} K (n_1 n_2)^{1/2} \sin\phi, \tag{6}$$

$$\frac{\partial \theta_1}{\partial t} = -\frac{K}{\hbar} \left(\frac{n_2}{n_1}\right)^{1/2} \cos\phi + \frac{e^* V}{2\hbar} \tag{7}$$

and

$$\frac{\partial \theta_2}{\partial t} = -\frac{K}{\hbar} \left(\frac{n_1}{n_2}\right)^{1/2} \cos\phi - \frac{e^* V}{2\hbar}. \tag{8}$$

From equations (5) and (6), we can easily find the transfer rate of the pair density equal to the transfer rate due to the flow of the Cooper pairs from one side to the other one. The equation (5) gives the current density from superconductor "2" to "1" and the Josephson current is as follows:

$$J = J_c \sin\phi, \tag{9}$$

where J_c is the critical current density of superconductors. J_c can be derived from microscopic theory and expressed by

$$J_c = \frac{G_n}{A} \left(\frac{\pi \Delta(T)}{2e}\right) \tanh \frac{\Delta(T)}{2k_{\mathrm{B}} T} \tag{10}$$

where G_n is the normal state tunneling conductance, A is the junction area, k_{B} is Boltzmann's constant and $\Delta(T)$ is the energy gap at the temperature T. We show a typical example of a tunnel junction's IVC (current-voltage characteristic) curve at T=0 in Fig. 3 (a). The gap voltage V_{g} is $2\Delta/e$ and normal state current I_{n} is indicated by the dashed line in Fig. 3(a). It is noted that the I_{c} equals the I_{n} at $\pi/4$ of V_{g}.

Fig. 3(b) shows the temperature dependence of I_{c} of Pb-Pb(oxide)-Sn and Sn-Sn(oxide)-Sn Josephson junctions. The solid lines are calculated by the equation (10) and the circles and squares are the experimental data points [11]. We can easily find that the I_{c} is getting smaller as the temperature becomes larger.

Josephson further predicted that when there is a voltage difference between the two superconductors, the Cooper pair should oscillate between them. By subtracting equation (7) from (8) and setting $n_1 = n_2$ for identical superconducting materials, we have the time-dependent phase difference across the junction:

$$\frac{\partial \phi}{\partial t} = \omega_{\mathrm{J}} = \frac{2e}{\hbar} V. \tag{11}$$

Here, we put $e^* = -2e$ because e^* is the charge of the two paired electrons. This effect means that when a Josephson junction is biased by a dc-voltage, we obtain electromagnetic (EM)

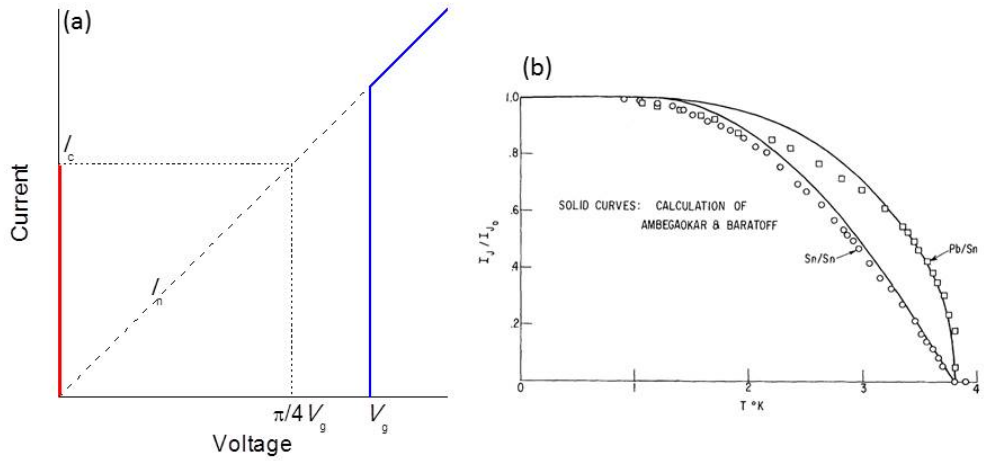

Fig. 3 (a) The typical image of IVCs (current-voltage characteristics) of a tunnel junction. (b) The experimental data and theoretical temperature dependences of the I_c of Pb-Pb(oxide)-Sn and Sn-Sn(oxide)-Sn Josephson junctions [11]. I_c grows with decreasing temperature.

waves whose frequency, $f = \omega_J/2\pi$, is proportional to the biased voltage per single Josephson junction. For example, when a single Josephson junction is biased at 1 mV, an EM wave with the frequency, f=483.597 852(5) GHz is generated [12].

2.2 Various Josephson junctions

In the previous section we derived the most important two relations: the dc- and ac-Josephson effects, *i.e.*,

$$I = I_c \sin\phi \ , \text{ and } f_J = \frac{2e}{h} V.$$

where f_J is the ac-Josephson frequency of the emitted EM wave. Both relations have been used in a wide variety of fields of applications such as SQUIDs (Superconducting Quantum Interference Devices), the voltage standard, the measurements of elementary charge and quantum computation devices, *etc.*

Josephson junctions as originally proposed by Josephson, are based on the quantum mechanical tunneling through the thin insulating barrier, which is placed between the two planar superconductors. However, it turned out that the effect can occur in many more cases and the concept can be extended more widely whenever two superconductors are connected by the weak links such as a narrow strip or constriction, *etc.* Several examples of Josephson junctions are illustrated in Figs. 4(a) $\sim$ (d). Figure 4(a) is a sandwich type of Josephson junction that

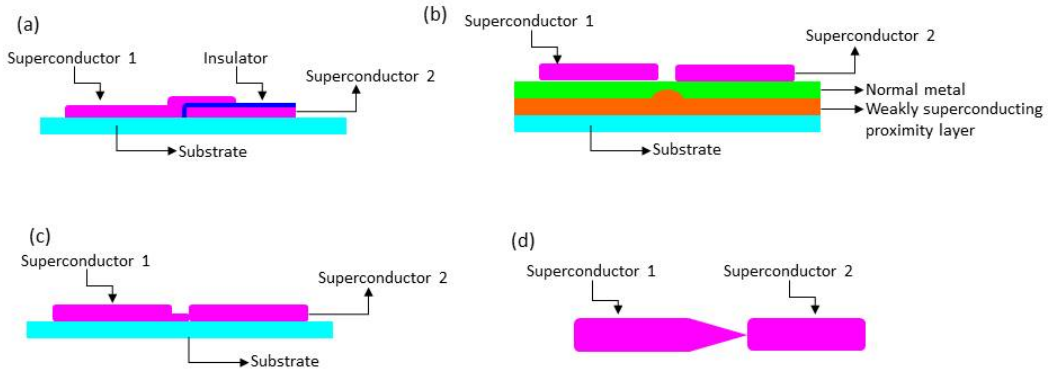

Fig. 4 The various Josephson junctions. (a) A sandwich type Josephson junction originally proposed by Josephson. (b) A two dimensional Josephson junction. (c) A constriction type of Josephson junction. (d) A point contact type of Josephson junction.

Josephson originally proposed. An example of the barriers between two superconductors may be an insulator with the thickness of a few nm, a degenerate semiconductor with the thickness of ~ 0.1 μm, which shows a metallic-like behavior or a metal layer with a thickness of ~ 0.5 μm, *etc.* As seen in the other cases in Fig. 4, for example, the superconducting electrodes are arranged in a form of two dimensional planes as shown in Fig. 4(b) so that both electrodes are separated by sub-micron thickness of gaps coupled by the so-called proximity effect. Sometimes, the weak link can simply be a narrow constriction (Fig. 4(c)) or a point contact (Fig. 4(d)). The constriction may be fabricated by the same superconducting material with much smaller cross section for the current as seen in Fig. 4(c). In the case of a point contact, the coupling is made by a needle-like connection through an oxide barrier or some microscopic sharp tip contact as shown in Fig. 4(d). Since the coupling strength can be tuned by adjusting the pressure on the point, this point contact type of Josephson junction is useful for some applications.

2.3 Current-Voltage characteristics (IVCs) with a dc source

The IVCs of a Josephson junction with a dc current source is usually understood by the RCSJ (Resistively and Capacitively Shunted Junction) model. The equivalent circuit for a current flowing the Josephson junction can be represented by a capacitor, C, and the sum of the quasi-particle tunneling current, $I_c \sin\phi$, and the leakage currents through an insulator with a voltage dependent conductance, $G = 1/R$, as shown in Fig. 5. The differential equation

for the circuit is represented as follows:

$$I = I_{\rm c}\sin\phi + \frac{V}{R} + C\frac{{\rm d}V}{{\rm d}t}. \tag{12}$$

By substituting equation (11) into (12), we have

$$I = \frac{\hbar C}{2e}\frac{{\rm d}^2\phi}{{\rm d}t^2} + \frac{\hbar}{2eR}\frac{{\rm d}\phi}{{\rm d}t} + I_{\rm c}\sin\phi. \tag{13}$$

When the equation (12) is divided by $I_{\rm c}$ and t is replaced by

$$\theta \equiv \omega_{\rm c} t \equiv \frac{2e}{\hbar} I_{\rm c} R t, \tag{14}$$

where $\omega_{\rm c}$ is the Josephson angular frequency at $I_{\rm c}$ (see equation (11)), we obtain

$$\frac{I}{I_{\rm c}} = \beta_{\rm c}\frac{{\rm d}^2\phi}{{\rm d}\theta^2} + \frac{{\rm d}\phi}{{\rm d}\theta} + \sin\phi, \tag{15}$$

where

$$\beta_{\rm c} = \omega_c C R = \frac{2e}{\hbar} I_{\rm c} C R^2. \tag{16}$$

The behavior of IVCs depends on $\beta_{\rm c}$. In the case of coplanar type of junction (see Fig. 4(b)), since the capacitance is very small, $\beta_{\rm c}$ is nearly equal to 0. When β is zero, V is zero below $I_{\rm c}$ and IVCs draws the parabolic curve above $I_{\rm c}$ as shown in Fig. 6. On the other hand, like in the case of Fig. 4(a) when $\beta_{\rm c} = \infty$, where C is very large, IVCs show a straight line as seen in Fig. 6.

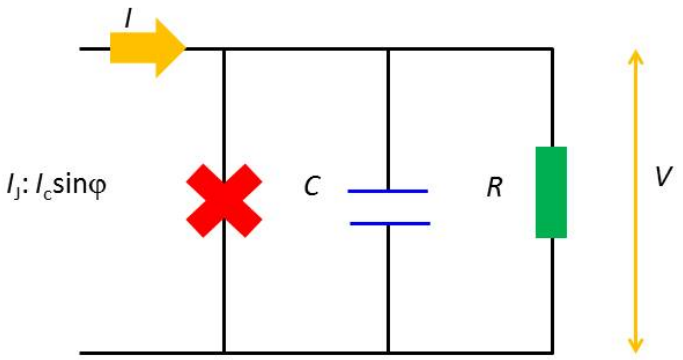

Fig. 5 The equivalent electrical circuit of the Josephson junction in the RCSJ model

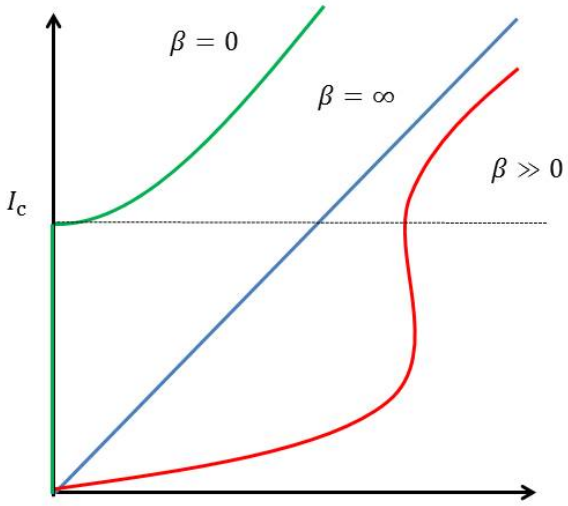

Fig. 6 The IVCs in the case of $\beta = 0, \infty$ and $>> 0$

However, the intermediate situation where $0 << \beta_c << \infty$, they behave completely differently from both of those limiting cases ($\beta_c = 0$ and ∞) and become more complicated but interesting. In order to understand the intriguing behaviors of IVCs exhibiting the complex nonlinear phenomena, in particular let us consider a *tilted washboard analog* as shown in Fig. 7. The junction dynamics described by equation (13) is mathematically identical to the motion of the round ball rolling down a washboard-like hill in a viscous fluid. Here, the average slope, ripples and mass of the ball correspond to the bias I, $I_c \sin\phi$, C and the energy storage factor: $(\frac{\hbar}{2e})^2$, respectively. The drag by the viscous fluid corresponds to R.

If the slope of the wash board is zero, which corresponds to $I = 0$, the ball is at rest initially. When the slope is gradually increased but not too much, the ball is still trapped by the washboard ripple, which corresponds to the IVCs at $I < I_c$. Therefore, below I_c, V is zero. Finally, the slope becomes sufficiently large for the ball to start rolling down. This critical slope corresponds to I_c and their situation is the same as an appearance of the voltage by an abrupt jump just above I_c as shown in Fig. 6 . After that, the ball will reach the average voltage which corresponds to the dc-voltage (linear behavior in the higher current region). Although the slope decreases after the ball starts rolling down, and the ball continues rolling because of its inertia. Therefore, even if I becomes smaller than I_c after an abrupt voltage jump occurs, the current does not become zero immediately and the IVC draws a hysteresis curve with Joule heating as shown in Fig. 6.

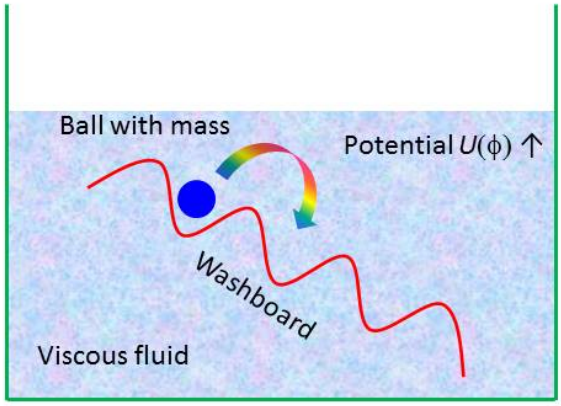

Fig. 7 The *tilted washboard analog* model of IJJs. The behavior of the IVCs of Josephson junctions can be described by the tilted washboard analog model and a ball rolling down.

2.4 The historical aspect of the ac-Josephson effect

Here, I would like to highlight some important historical aspects of the ac-Josephson effect. As was mentioned in section 2.1, Brian D. Josephson predicted the ac-Josephson effect when a potential difference between two superconductors is realized across a Josephson junction. This means that part of the superconducting current will oscillate back and forth between the two superconductors through the thin barrier at a frequency of $f_{\rm J} = 2eV/h$ (ac-Josephson effect), where V is the voltage appearing between two superconductors, e is the magnitude of the elementary charge of an electron and h is the Planck constant.

This ac-Josephson effect was indirectly confirmed by S. Shapiro and others [13] in 1963 using a microwave technique. When a Josephson junction is irradiated by an EM wave with the angular frequency ω_1, the induced supercurrent by the EM wave gives rise to a voltage $V_n = n\hbar\omega_1/2e$, where n is a positive integer. This is called the "Shapiro step", and is shown in Fig. 8. The appearance of these steps in IVCs was interpreted as the modulation effect of the ac-Josephson current excited by the external radiation.

Now, let us consider this phenomenon in more detail. First, we take the bias voltage to be

$$V = V_0 + V_1 \cos\omega_1 t. \tag{17}$$

By substituting equation (17) into (11), the phase difference becomes

$$\phi = \frac{2e}{\hbar} V_0 t + \frac{2eV_1}{\hbar\omega_1} \sin\omega_1 t + \text{Const.} \tag{18}$$

Inserting equation (18) into (9) and defining $\omega_0 \equiv 2eV_0/\hbar$, we have

$$I_{\rm s} = I_{\rm c} \sum_{n=0}^{\infty} (-1)^{\rm n} J_{\rm n}(2eV_1/\hbar\omega_1) \sin(\text{Const} + \omega_0 t - n\omega_1 t), \tag{19}$$

where $J_{\rm n}$ is the n-th Bessel function of the first kind. Here, to avoid confusion, we substitute $J_{\rm s}$ for $I_{\rm s}$ as the term for the supercurrent density. It turns out that it contributes a dc component only when $\omega_0 = n\omega_1$. Therefore, the Shapiro step values can be expressed as follows:

$$V_n = n\hbar\omega_1/2e. \tag{20}$$

After the indirect observation of ac-Josephson effect by S. Shapiro *et al.*, several results of investigations were reported that the step-like structure occurs in IVCs of Sn-I-Sn tunnel junctions without external radiation (I in Sn-I-Sn means an insulator). This phenomenon strongly suggested the excitation of EM oscillations inside the Josephson junction. In fact, Svistunov and Yanson firstly succeeded in detecting the photon emission at the frequency satisfying the Josephson relation by using a tunnel junction (Sn-Sn0_2-Sn) [14]. However, since

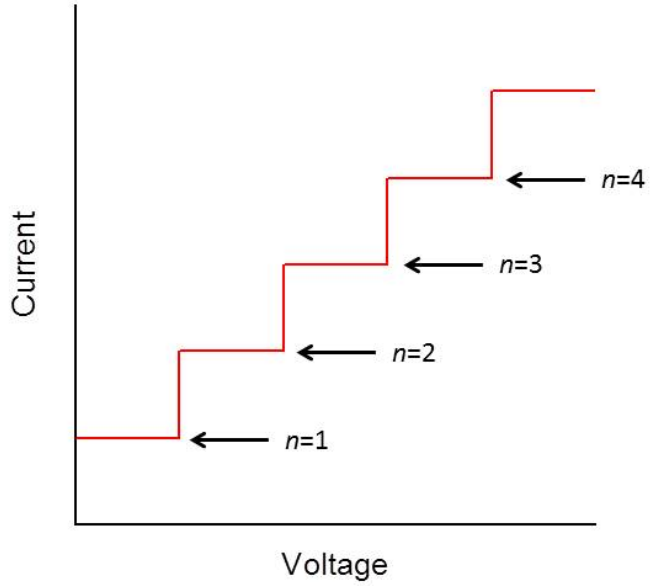

Fig. 8 The image of the first to the 4th Shapiro steps in the IVCs.

the radiating emission power from a single Josephson junction is very weak and was only at the 10 pW level at 9.2 GHz, it was difficult to detect the ac-Josephson effect directly. It was not useful to think of it as an emitter at that time.

In the 1980s and 1990s, one and two dimensional array structures of Josephson junctions was developed to make synchronized operations to obtain coherent radiation [15]. In order to synchronize the junctions, it is required to fabricate the array to be smaller than the radiation wave length. In this case, the synchronized operation was understood as a result of the interaction between junctions and electromagnetic field. In 1999, P. Barbara *et al.*, succeeded in detecting 150 GHz microwave radiation by two-dimensional Josephson junction arrays, whose size is about 2 mm in length, which is comparable to the wave length of free space radiation [16]. The size of the array is much larger than those of classical ones [15]. They first showed that a large array structure with many Josephson junctions can emit coherent radiation as a laser (light amplification by stimulated emission of radiation). Furthermore, they reported the ac power conversion rate from dc input power is about 17%, which is one to two orders of magnitude higher than obtained from previous clasical junction arrays.

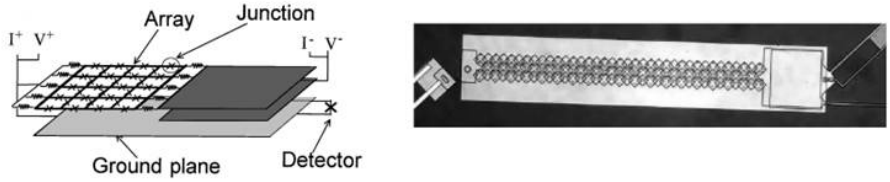

Fig. 9 The schematic illustration (left) and the photo (right) of the two-dimensional array structure of Josephson junctions [16].

3 High-T_c superconducting $Bi_2Sr_2CaCu_2O_{8+\delta}$ single crystals

3.1 Confirmation of the intrinsic Josephson effect in Bi2212 single crystals

In the previous section 2.4, the coherent EM waves from a two dimensional array structure of Josephson junctions were mentioned [16]. However, there has been a great difficulty to fabricate identical arrays of two dimensional Josephson junctions that synchronize coherently. In contrast to this, high-T_c superconductor $Bi_2Sr_2CaCu_2O_{8+\delta}$ (Bi2212) single crystals have been expected to possess discrete superconducting layers separated by the insulating Bi_2O_2 and SrO layers acting as a Josephson junction as shown in Fig. 10. The first experimental evidence was demonstrated by R. Kleiner *et al.* [17] by the IVC measurements of Bi2212 single crystal along the c-axis direction at 4.2 K. The typical dimensions of the sample were 30 x 30 μm^2 in the ab-plane and 3 μm in the c-axis direction ($\sim$ 2000 junctions). Applying

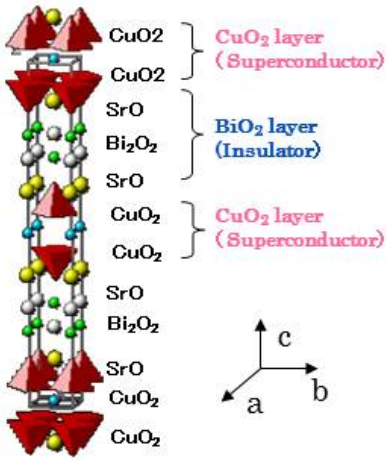

Fig. 10 The crystal structure of $Bi_2Sr_2CaCu_2O_{8+\delta}$ (Bi2212) single crystal.

a dc current higher than the critical current I_c, they showed many new branching structures in the IVCs of such a small mesa sample. When the bias current I is decreased from the voltage state in one of the IVCs, the voltage decrease continues until it jumps back to zero as shown in Fig. 11(a). They observed many separated IVCs and discerned more than a hundred different branches, which are almost equally spaced as seen in Fig. 11(a). From such observations, it was understood that the multi-branch structure in the resistive state is due to the repeatedly connected number of junctions, and therefore, the Bi2212 single crystals were proved to contain intrinsic Josephson junctions along the c-axis direction.

Furthermore, they succeeded in observing the EM waves from the Bi2212 sample in the resistive state. The emission by the spectral investigation is indicated in Fig. 11(b). Since the line width of the emission spectra in the N synchronized system is expected, show a decrease linearly with increasing N, the experimental result shown in Fig. 11 (c) can be interpreted as evidence of synchronize operation of N IJJs in a Bi2212 single crystal. Note that in the case of single Josephson junction, the line width becomes about 300 MHz typically. Since the line width of 50 MHz observed in their experiment seems to be much wider than the expected value in the $N \sim 2000$ system, they concluded that such a broad line width may come from the unlocked Josephson junctions which do not participate in radiation coherently. They estimated the number of phase-locked junctions to be of the order of 10, which are much smaller than the actual number of IJJ junctions involved in the Bi2212 mesa sample.

3.2 Josephson plasma excitation in Bi2212 single crystals

Plasma is considered as one of the four fundamental states of matter in addition to the conventional three states of matter: solid, liquid and gas, and it consists of the state in which electrons, ions or both of them are mixed and can move freely. The most well known plasma is a fusion plasma which can be obtained by burning deuterium or tritium at temperatures above several tens of million degrees. Since a metal is filled with free electrons, it can be viewed as the one of the plasma states. In such a plasma state in metals, the collective oscillation of electrons or ions exists and is called plasma waves or plasmons after quantization. Therefore, the collective oscillation of free electrons in turn can be considered to be a collection of plasmons.

Now, let us consider plasma phenomena in a superconductor since the collective plasma motion in a superconductor has the characteristic frequency $\omega_{\rm ps}(= 2\pi f_{\rm ps})$ called as the plasma frequency in the superconducting state, which is compared with the plasma frequency, $\omega_{\rm p}$, of the metal in the normal state. In a conventional metal, the Coulomb repulsive interaction energy of electrons in the metal lies on the order of $\sim eV$, *i.e.*, $E_{\rm plasma} = \hbar\omega_{\rm p} = \hbar e\sqrt{\frac{n}{m\varepsilon_0}}$ ($\simeq$10 eV) where $\omega_{\rm p} = e\sqrt{\frac{n}{m\varepsilon_0}}$ is the plasma angular frequency, n the density of electrons, ε_0 and m

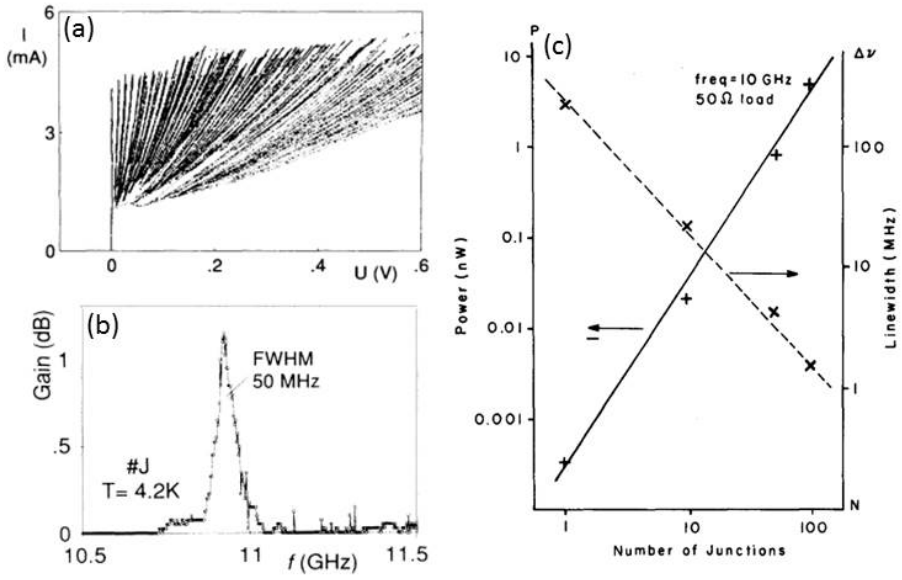

Fig. 11 (a) Multi branching structure obtained in the IVCs of Bi2212 single crystals. More than a hundred branches were seen [17]. (b) The EM wave with the line width of 50 MHz was detected at $T_{\rm b} = 4.2$ K [17]. (c) The N dependence of emission power and the line width of EM waves radiated from the synchronized Josephson junctions [15]. The line width of radiation decreases with increasing N, where N is the number of the IJJs involved in the radiation.

are the permitivity (dielectric constant of vacuum) and the electron mass, respectively.

Similarly, the plasma energy in the superconducting state can be expressed as $E_{\rm ps} = \hbar\omega_{\rm ps} = \hbar e\sqrt{\frac{n_{\rm s}}{m\varepsilon}}$, where $n_{\rm s}$ means the density of superconducting electrons, *i.e.*, the density of Cooper pairs in the superconducting state, ε is the effective dielectric constant in the superconducting state. On the contrary to the metallic plasma energy scale, the superconducting energy scale can be described by the superconducting gap energy, Δ, in the superconducting state. In conventional superconductors, Δ is only on the order of a few meV. Even in high-$T_{\rm c}$ superconductors, it is only below ~ 40 meV, which is much less than the metallic plasma energies $\hbar\omega_{\rm p}$. Therefore, the superconducting plasma can not be differentiated from the normal state plasma even if the superconducting plasma does exist. This is the reason why the superconducting plasma state can not be observed directly by the optical excitation method or any other experimental means in conventional superconductors.

This situation dramatically changes in the case of Josephson plasma in high-$T_{\rm c}$ superconductors. Here, the Josephson plasma means that the Josephson current flowing in between two superconductors coupled with the weak Josephson interaction, can play a role as the

superconducting plasma, where the Josephson critical current density, $J_{\rm JC}$ as a limitation of superconducting current flow in the Josephson junction, is much less than that of the superconductors. This was first argued by P. W. Anderson [18] soon after the discovery of the Josephson effect by B. D. Josephson in 1962 [8]. According to him, as a Cooper pair tunnels through a thin barrier from one superconductor to the other, the phase difference $\phi = \theta_1 - \theta_2$ is created. This induces the increase of energy, $\Delta E(\phi)$,

$$\begin{aligned}\Delta E(\phi) &= E(1-\cos(\phi)) \\ &= \frac{\hbar J_{\rm JC}}{2e}(1-\cos(\phi)),\end{aligned}$$

where $J_{\rm JC}$ is the Josephson current density. After moving a Cooper pair from one superconductor to the other, what happen in the system? Because two electrons were transfered from superconductor "1" to "2", superconductor "2" has two more charges, $2e$, than superconductor "1", resulting in the charge unbalance between two superconducting electrodes "1" and "2". This causes an increase of static Coulomb energy $\Delta(\delta_n)$, which can be expressed as

$$\Delta E(\delta_n) = \frac{(\delta Q)^2}{2C} = \frac{(2e\delta_n)^2}{2C},$$

where, $C = \varepsilon/4\pi d$ is the capacitance of the Josephson junction, δQ and δ_n mean the net changes and the number of Cooper pairs moved from "1" to "2", respectively. Here, ε is the dielectric constant of the insulator between two superconductors. Therefore, the Hamiltonian per unit area can be written as,

$$\begin{aligned}H &= \frac{(\delta Q)^2}{2C} + E(1-\cos\phi) \\ &= \frac{(2e\delta_n)^2}{2C} + \frac{\hbar J_{\rm JC}}{2e}(1-\cos(\phi)).\end{aligned}$$

It is interesting to note that this Hamiltonian is mathematically equivalent to that of a harmonic oscillator with the momentum δ_n and the coordinate ϕ. Therefore, the eigen frequency $\omega_{\rm ps}$ corresponding to the harmonic oscillator can be written by

$$\hbar\omega_{\rm ps} = \sqrt{\frac{(2e)^2 E}{C}} = \sqrt{\frac{2ed\hbar J_{\rm JC}}{\varepsilon}}.$$

This equation can be rewritten as

$$\omega_{\rm ps}^2 = \frac{2edJ_{\rm JC}}{\varepsilon\hbar} = \left(\frac{1}{\lambda_{\rm J}}\right)^2 \frac{1}{\varepsilon}$$

where $\lambda_{\rm J} = \sqrt{\frac{\hbar c}{2eJ_{\rm JC}d}}$, which is the Josephson penetration depth. Therefore, the value for the Josephson plasma frequency can be deduced to $\omega_{\rm ps} = 2\pi f_{\rm ps} = 3.3\text{x}10^{11}$ rad/sec, which corresponds to $\simeq 53$ GHz.

Since this Josephson frequency, $\omega_{\rm ps}$, is on the order of a few 100 GHz, the energy to excite the Josephson plasma must be only 0.43 meV or above, which is well below the superconducting energy gap of $\Delta \simeq 40$ meV in the case of high-$T_{\rm c}$ superconductors. Because of this unusual energy relation, the Josephson plasma can be excited in the superconducting state inside the superconducting gap. Since the excitation occurs inside the superconducting gap, there is no damping mechanism such as the Landau damping for the quasi particles. Therefore, the excited plasma mode can survive for a very long time without damping, resulting in the sharp excitation spectrum as observed in microwave absorption experiments. This excitation mode indeed was discovered for the first time by Matsuda *et al.* in the microwave frequency region[19], although the same phenomena was observed by O. K. C. Tsui *et al.* [20] in a similar experiment. They interpreted the magnet optical absorption as an anomalous skin effect of the microwave in the high-$T_{\rm c}$ superconductor Bi2212, and misunderstood the phenomena as an anticyclotron resonance effect, unfortunately.

The correct theoretical interpretation of the above microwave absorption phenomena observed in high-$T_{\rm c}$ superconductor Bi2212 single crystal was given by Tachiki *et al.* [21, 22, 23]. The key observation in experiments to inspire him and lead him to the correct interpretation was the sharp microwave absorption spectrum, which is observed only when the crystal is set in a special position inside the microwave cavity resonator. In other words, the microwave absorption can be induced only when the electric field, $E_{\rm rf}$, of the microwave is extended parallel to the c-axis of the Bi2212 crystals. According to the work done by Tachiki *et al.*, this means that the longitudinal Josephson plasma mode is excited in such a configuration of microwave $\boldsymbol{E}_{\mathbf{rf}}$ vector. Furthermore, they predicted other two modes propagating along the ab-plane in Bi2212 single crystals, which are the transverse modes. In this case, the microwave magnetic field $\boldsymbol{H}_{\mathbf{rf}}$ should be applied parallel to the superconducting ab-planes.

These particular properties can be used for the separation of the plasma modes as follows, tested by the microwave experiments mentioned above. In fact, such a distinction between the two different plasma modes existing in a Bi2212 single crystal has been done using the microwave technique by the group of Prof. Kadowaki in the University of Tsukuba [24, 25, 26]. Following the theoretical prediction, the longitudinal Josephson plasma mode can be observed, when the microwave electric field vector, $\boldsymbol{E}_{\mathbf{rf}}$, is applied parallel to the c-axis of the Bi2212 single crystal, whereas the transverse Josephson plasma mode can be observed, when the microwave magnetic field vector, $\boldsymbol{H}_{\mathbf{rf}}$, is applied parallel to the surface of the ab-plane of the Bi2212 single crystal. These experimental conditions can be found in ref. [27], where a rectangular cavity resonator with $\rm TE_{102}$ mode is constructed in such a way that the single crystal sample can be placed at different positions in the same cavity resonator for performing either longitudinal or transverse plasma resonance measurements [27]. The frequency range between 25 GHz and 70 GHz were used for the above experiments.

The importance of these microwave absorption experiments lies not only in the study of the Josephson plasma phenomena themselves in a superconducting state for the first time, but by changing the experimental conditions to be excited by microwaves not only the absorption phenomena with a variety of experimental conditions such as applied magnetic fields and the angular dependence of the magnetic field applied to the sample, temperature, external currents, *etc.* but also in more fundamental aspects of superconductors. Since the microwave absorption phenomena are in general reverse processes of emission phenomena in quantum mechanics, it is expected that electromagnetic (EM) waves can be extracted from a Josephson junction, if the Josephson plasma is excited in the Josephson junction by some means, for example, by flowing dc-current to the junction. As was already mentioned, although direct and indirect detection of electromagnetic radiation have indeed been done using classical Josephson junctions [14], similar experiments may be extremely interesting because of the inherent multi-junction nature of IJJs, promissing an enormous power enhancement according to $P \propto N^2$. Furthermore, the fabrication process must be much easier in the case of IJJs than the conventional superconducting arrays because the individual Josephson junctions in the single crystal are in a perfect state as long as the quality of the single crystal is good enough. In the following, we summarize the advantage of using the high-T_c superconducting Bi2212 single crystals as an emitter of EM waves.

They are

1. Fundamentally, the mechanism of EM wave emission is different from the conventional EM emission. It is continuous and coherent emission.
2. Much higher frequency can be generated, which can not be reached by the conventional Josephson junction because of much higher superconducting gap energy in high-T_c superconductors, approximately ten times larger in the gap energy than for the conventional Josephson junctions. This advantages can not be taken by any other devices based on semiconductor technology and optical means except for RTD and QCL.
3. Much stronger emission can be obtained from high-T_c superconductors than from conventional Josephson junctions arrays, since the intensity of radiation must be proportional to N^2, where N is the number of Josephson junctions coupled together by synchronization. This leads to some tens of micro watts level of power, much greater than the pW power of a single layer Josephson junction.

These three major advantages are certainly strong reasons to push us toward higher emission intensity and higher emission frequency devices using high-T_c superconductor Bi2212. We believe that it is probably possible to reach above 1 mW level of emission power and several THz range of frequency by improving the device performance using our knowledge obtained here, in particular, concerning thermal management. There will also be another direction

to enhance power greatly using arrays of mesas and operating them coherently. Research work along such lines is in progress in the Kadowaki-Kashiwagi, and the Minami Lab. at the University of Tsukuba.

4 Strong THz radiation from Bi2212 mesa device

In 2007, the Kadowaki group at the University of Tsukuba, Japan, in collaboration with Dr.Wai Kwok and Dr.Ulrich Welp at Argonne National Laboratory in the USA, discovered the THz emission from a compact mesa structure fabricated from high-T_c superconductor $Bi_2Sr_2CaCu_2O_{8+\delta}$ (Bi2212) single crystals [7]. The most important parts of their report were extracted from the original publication as shown in Fig. 12. They found two important requirements for the THz radiation: one is the ac-Josephson effect, which is described in the former section [8] and is actively working while the mesa is emitting the THz radiation. The other one is the cavity resonance effect, which considerably enhances the emission intensity at certain cavity resonance frequencies determined by the geometrical conditions such as the

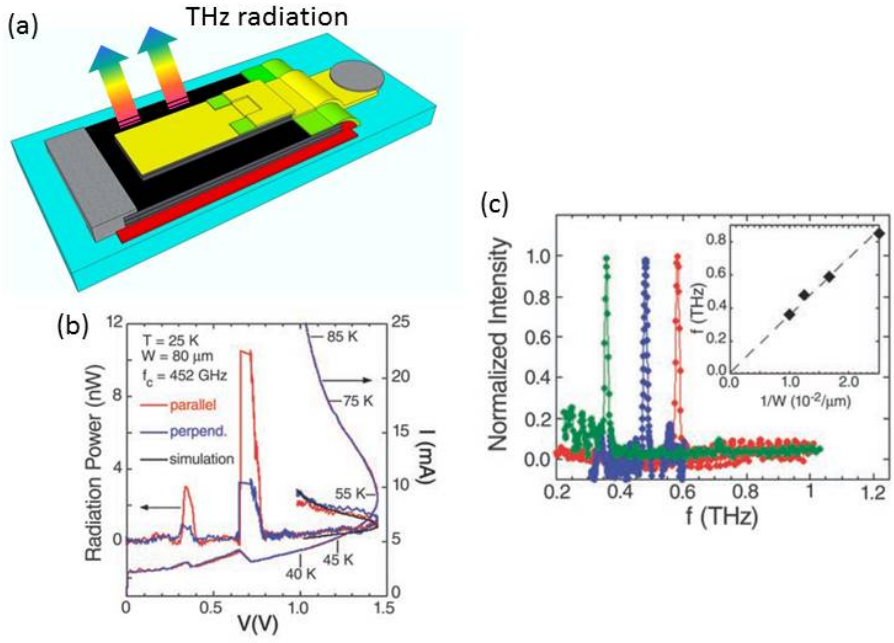

Fig. 12 (a) Schematic drawing of the rectangular Bi2212 THz emitting device. (b) The IVCs of the rectangular Bi2212 THz emitting device 80 μm in width and the emission intensity *vs.* bias voltage, V. The strong and sharp peak representing THz radiation was observed at the lower bias current, I, and in the far IR region (actually in a THz region) at 25 K. [7]. (c) The normalized emission intensity *vs.* radiation frequency, f, emitted from rectangular mesa structures 100 μm (green), 80 μm (blue) and 60 μm (red) in width [7].

shape of the mesa: for example, rectangular, square, circular mesa structures, *etc.* and their dimensions [28]. In the case of a rectangular mesa with the width, w, the lowest resonance frequency, $f_{\rm r}$, obeys the condition that $f_{\rm r} = c_0/2nw$, where c_0 is the velocity of light in vacuum and n the refractive index of the superconductor. Strong THz emission is expected to occur when both this and Josephson conditions are satisfied at the same time. After their discovery, intensive studies have been carried out continuously until today. Figure 12(c) shows the normalized emission power emitted from three rectangular mesa devices with w = 60, 80 and 100 μm [7]. As seen in Fig. 12(c), the emission frequency f increases with decreasing the width w. The inset of Fig. 12(c) shows more clearly that f is proportional to $1/w$, strongly suggesting that the resonance enhancement of the THz waves, *i.e.*, the standing wave in the rectangular mesa with the resonance frequency $f = f_{\rm r}$ occurs along the width, not along the length.

5 Joule heating effect of Bi2212 THz emitting devices

In the recent few years, in particular, the development of the Bi2212 THz emitting devices has been remarkable. The emission power has reached reproducibly up to $30 \sim 50$ μW per mesa [30, 31, 32] and more than 600 μW was reached for three synchronized mesa operation together [29]. The maximum emission frequency of 2.4 THz was also reported recently [33]. Such a remarkable advancement has been achieved based on the results of serious studies of the Joule self-heating problem and its proper understanding, in spite of complicated and cumbersome problems because they are inhomogeneous, non-equilibrium and dynamical phenomena. In this section, we would like to summarize the results of the Joule-heating problem of the Bi2212 THz emitting devices so far reported in the past several years. In fact, three previous works gave me a strong motivation to start my Ph.D. study.

5.1 Experimental observation and the theoretical simulations of the hot spot

Concerning the Joule heating problem, Wang *et al.* first showed results of the thermal image of the mesa device made from a Bi2212 single crystal during THz emission, observed by the low temperature scanning laser microscope (LTSLM) technique [34, 35, 36]. The LTSLM technique can detect the voltage change, ΔV, caused by the change of local temperature induced by the focused laser beam, which warms up the sample locally by a few K. This method allows for the visualization of the electric field and current distributions with a lateral resolution of some micrometers. Using this method, they deduced the somehow clear image of the temperature distribution after conversion of the ΔV images observed in Fig. 13(c) as the bright circular image, to the temperature distribution images by using some numerical calculations. This sort of local high temperature spot called a "hot spot" was clearly seen in the mesa at higher current regions. The important point in this measurement is that the THz emission was observed even in such a huge temperature inhomogeneous state with the "hot spot", whose temperature is known to be even higher than $T_{\rm c}$ of this Bi2212 compound [34, 35].

They further pointed out the formation of the standing wave pattern in the rest of the superconducting part beside the hot-spot image as seen at the right hand side of Fig. 13(c), when the mesa is radiating the EM waves, and they claimed that the hot spot works as a node of the standing wave as if it were the normal state wall against the standing wave because the hot-spot region is in the normal conducting state having temperature, T, well above $T_{\rm c}$. The ac-Josephson effect no longer works there so that they assume that the boundary between the hot spot and the superconducting region may work as a reflecting wall of the standing

waves. They further claimed experimental observation as evidence that the emission frequency changes when the size of the cold part of the mesa (*i.e.*, the position and the size of the hot spot) is changed. Based on the experimental results shown in Fig. 13, they supposed that the wavy pattern may be reminiscent of the THz standing wave. Since they think that the observed emission of THz radiation is generated by the standing wave, they believe that the hot-spot formation might be critically essential and even beneficial to the synchronization operation of the many stacked IJJs. Critically speaking from our point of view, the images shown in Fig. 13 (c) are not the ones obtained by the direct temperature measurement but constructed from some voltage response images induced by the local heating of the focused laser beam, which is in fact not unambiguous. It appears rather unclear in its physical origin. Furthermore, their observation of the hot spot was not done at the same time as the THz emission was observed. Therefore, it is even less obvious whether or not there is a physically meaningful correlation between the hot-spot formation and the THz emission, and by the same token the radiation frequency. Since they interpreted their findings that the size of the hot spot controls the wave length of the THz standing wave, *i.e.*, THz radiation frequency, it could be changed largely by the size of the hot spot *i.e.*, the bias current level. It is obvious that since at higher bias currents, the size of the hot spot grows larger, that interpretation could cause the THz emission frequency to increase considerably as the bias current is increased. This phenomenon was not seen previously, and especially it sharply contradicts the previous studies done by Tsujimoto and others [28].

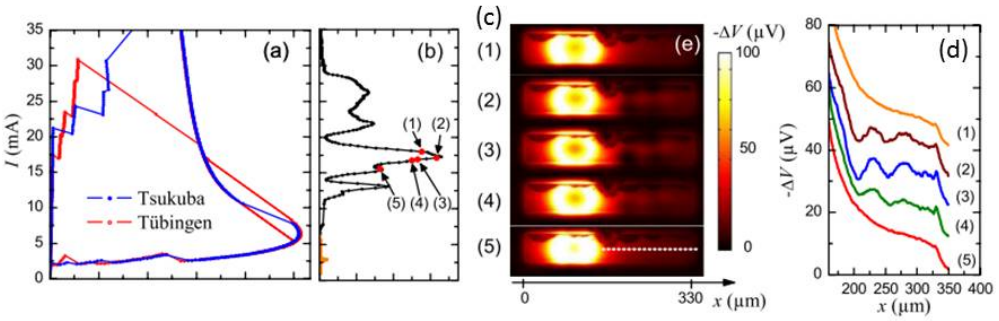

Fig. 13 (a) The IVCs at 20 K measured in Tsukuba and Tubingen by Wang *et al.* [34, 35]. (b) The emission intensity *vs.* the bias current, I. (c) The image of the electric field distribution (which is not convincing) measured by LTSLM method at the bias point (1) $\sim$ (5) indicated in Fig. 13(b) [34, 35]. (d) The line scans taken along the center of the mesa indicated by the dashed line in Fig. 13(c) [34, 35].

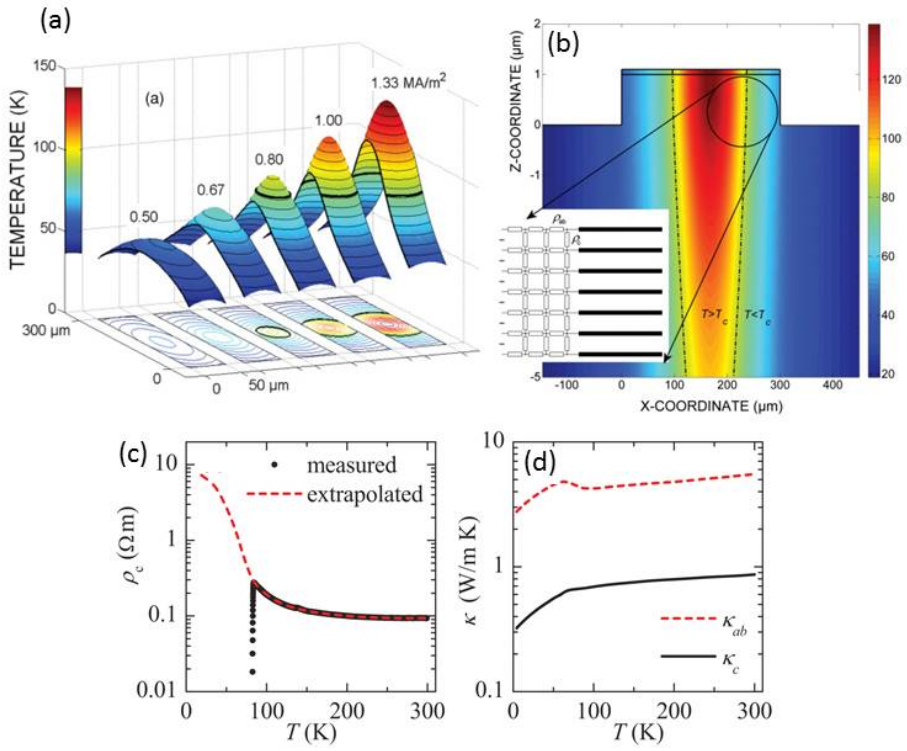

Fig. 14 (a) The computer calculated images of a "hot spot" in a Bi2212 THz emitting rectangular mesa device 80 μm in width. It had a sharp boundary between the superconducting region and the heated region. It is also well defined in the higher bias I region [37]. (b) The temperature distribution along the c-axis direction of the mesa on the superconducting substrate [37]. (c) The temperature dependence of the c-axis resistivity as measured (black symbols) and extrapolated by fitting the IVCs (dotted line) [38]. It shows a large negative temperature derivative. (d) Temperature dependence of the thermal conductivity of the Bi2212 in the ab-plane (red dotted line) and in the c-axis direction (black solid line) [38]. The c-axis thermal conductivity is much less than that of the ab-plane.

Soon after the results of Wang *et al*, Yurgens and others confirmed the formation of the hot spot by computer simulation as presented in Fig. 14 [37, 38]. They also came to the surprising conclusion that the temperature at the hot spot exceeds T_c of the Bi2212 superconducting mesa device, as mentioned by Wang *et al.* [34, 35]. They also wrote that the hot-spot size grows with increasing the bias current, I as seen in Fig. 13(c). Gross *et al.* attributed the appearance of the hot spot to the strongly negative temperature coefficient of the c-axis resistivity of Bi2212 single crystals at low temperatures, especially below about 50 K as seen in Fig. 14(c) [38].

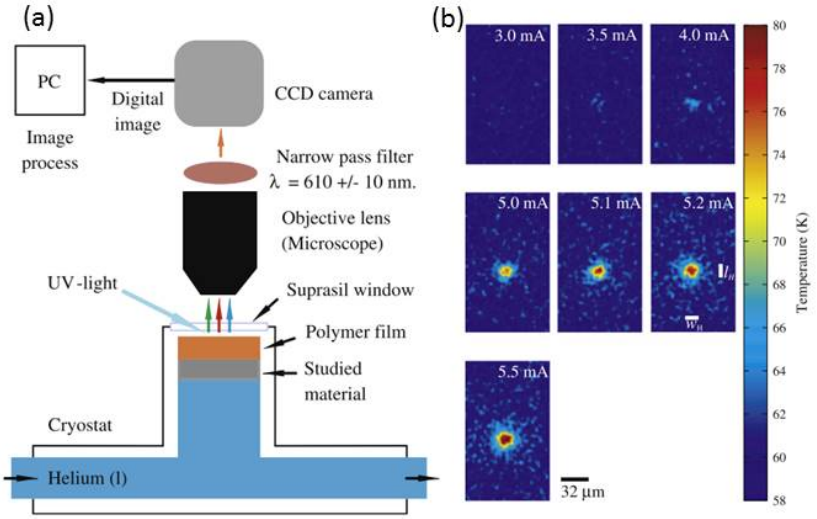

Fig. 15 (a) The experimental set up for measuring the device temperature using a fluorescent thermal imaging technique [39, 40]. (b) The clear and well-defined images of the hot spot on Bi2212 film are presented [39, 40].

5.2 Direct observation of the device temperature

As was discussed in the former section, 5.1, the device temperature can not be measured directly by the LTSLM technique. This appears to be the most serious defect of the LTSLM measurement technique. By choosing the other optical techniques for the temperature measurement, however this defect can be overcome. Here, the direct temperature measurement technique is summarized. The thermal imaging technique by optical means was introduced by Niratisairak *et al.* [39, 40]. They used a film of a rare-earth (containing Europium(III)) complex embedded in a polymer matrix as a thermal sensor. The experimental set-up used by them is indicated in Fig. 15 (a) [39, 40]. The film of a thermal sensor is deposited on the Bi2212 film and is irradiated with UV light. The film is excited and emits photoluminescent light, whose intensity shows a strong temperature dependence. As a result, with increasing temperature, the photoluminescent intensity becomes weaker. Using such a measurement technique, they succeeded in observing a clear image of the hot spot occurring in the Bi2212 film with high spatial and temperature resolution as shown in Fig. 15 (b).

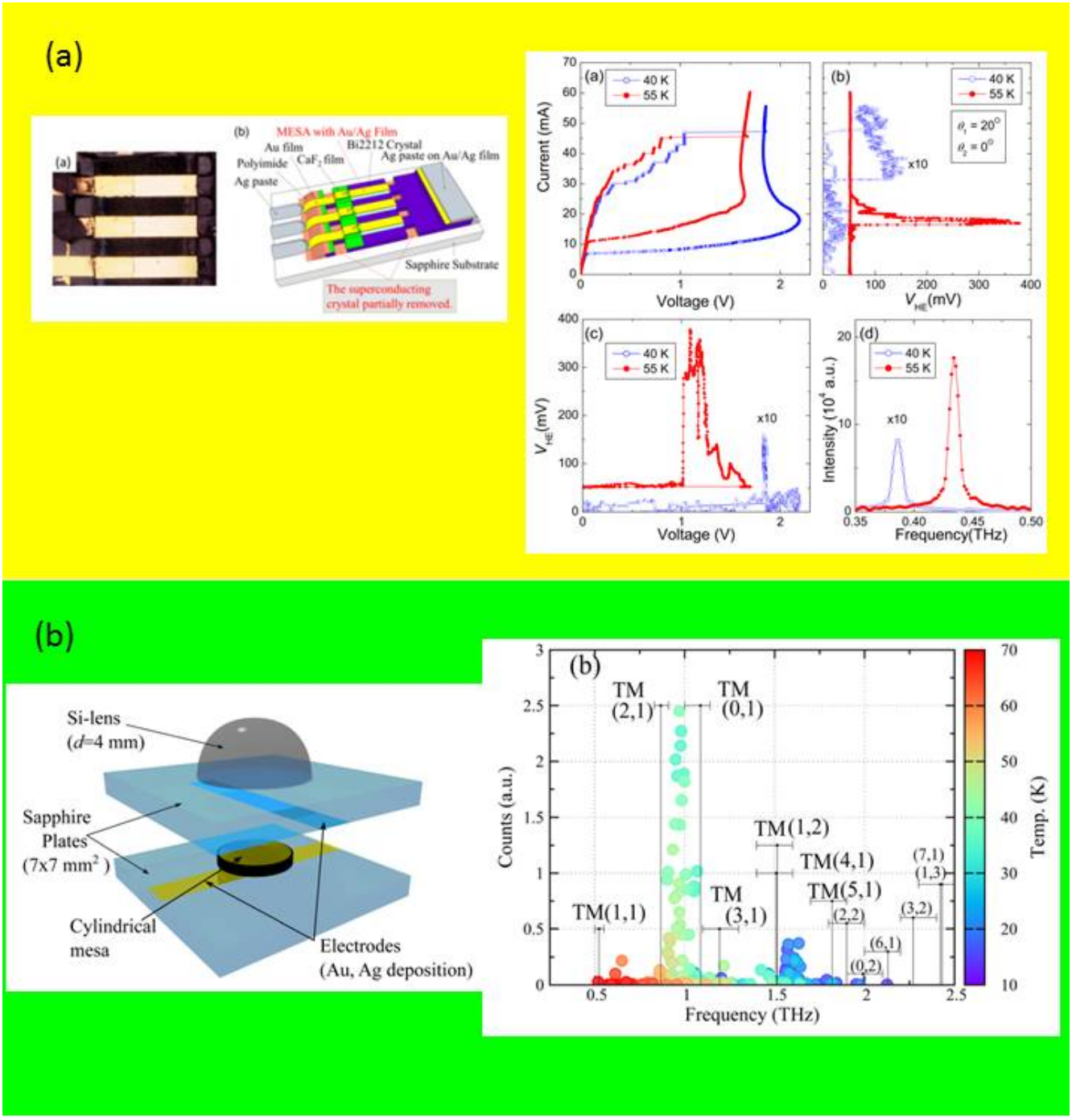

Fig. 16 The maximum emission intensity obtained from a single stand-alone type of mesa device. The mesa is made to have better cooling by partially removing the superconducting substrate [30]. The break-down structure of the stand-alone mesa is schematically displayed in the above, while in the below, the emission spectral intensity distribution collected from all emission peaks is plotted in one figure [33].

5.3 Joule heating effect of the Bi2212 THz emitting device on the emission character

In the former section 5.1, we discussed the previous studies of the hot spot experimentally and theoretically. As mentioned before, Wang *et al.* claimed that the hot spot may be beneficial to the THz emission [34, 35]. However, considering many experimental results so far obtained in our group, we doubted their interpretation based on incomplete experimental evidence, since they had not done direct temperature measurements and observations of the emission intensity simultaneously. We think that understanding the hot spot and its related phenomena are very important for the improvement of the THz emission towards higher power and higher frequencies. Here, we would like to show several studies to obtain better understanding of the influence of the Joule heating on the emission character. By studying the angular distribution of the radiation from rectangular and disk mesas, Klemm and Kadowaki proposed that the mesa should be removed from the Bi2212 substrate, and have the top and bottom surfaces covered with a metal such as gold [41]. The first Bi2212 mesa of this type was studied by Yamamoto *et al.* A modified device consisting of Bi2212 with gold with top and bottom surfaces, all of which was sandwiched between MgO plates, was studied by Zhou *et al.* [42], and emission up to 1.05 THz was obtained.

The strongest THz radiation intensity obtained from the single mesa device is so far about 30 μW (see Fig. 16(a)) [30] and the highest frequency is 2.4 THz (Fig. 16(b)) [33] observed, only when the mesa structure is well connected thermally with the thermal bath as shown in Figs. 16 (a) and 16(b). In the former case, the superconducting substrate under the mesa is much thinner than the ordinary structure so that the device works as if it were a stand-alone mesa. "Stand-alone" means no superconducting Bi2212 single crystal underneath the mesa structure. Indeed, the IVCs of this mesa sample behaves as a stand-alone type of mesa [33]. We note that the strongest radiation was observed in the lower current region, the so-called "retrap" region, where there is no hot spot even at low temperatures. In the latter case, the superconducting substrate was completely removed so that the THz emitting mesa device is covered with Au layers on the top and bottom and sandwiched between two sapphire plates. This structure is called a "stand-alone mesa sandwich device" [31, 44]. In such stand-alone type of mesas, the superconducting Bi2212 mesa itself was gently clamped in-between two MgO or sapphire plates in order to efficiently remove the Joule heating [31, 33]. These experimental results are very interesting to understand the hot-spot formation and the role of it for THz generation in IJJs in Bi2212 and may provide us with an important clue to obtain stronger THz radiation from intrinsic Josephson junction devices. Contrasting to the result of the LTSLM measurement, these results strongly suggest the possibility that the emission

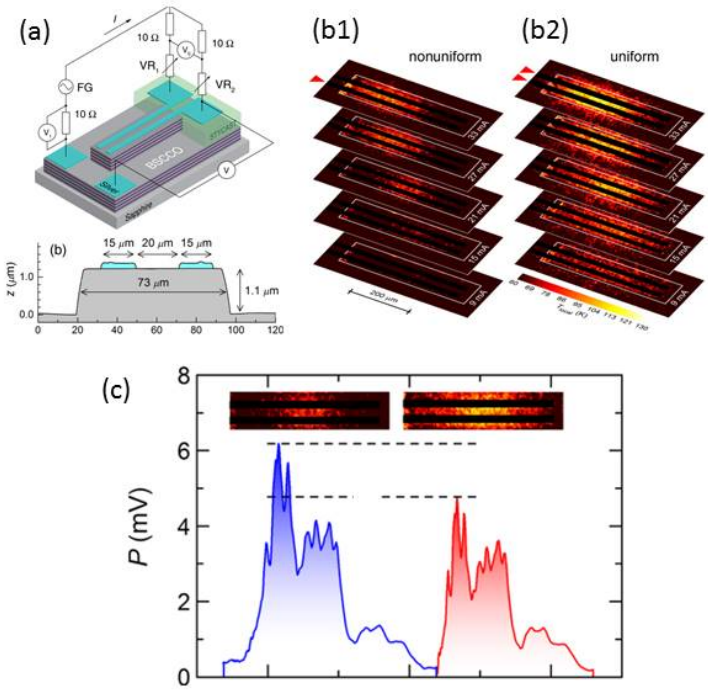

Fig. 17 (a) The schematic figure of the mesa device with two electrode terminals and the circuit to measure the IVCs [43]. (b) The images of the temperature distribution $T(r)$ in the case of non- and uniform bias [43]. (c) is the emission intensity in the case of non-uniform bias (blue) and uniform bias (red) respectively [43]. The emission intensity with less Joule heating is higher than that with large Joule heating.

intensity may be drastically improved by removing the Joule heating that causes a hot spot *i.e.*, by preventing hot-spot formation in the device. This suggestion is in a sharp contrast with the interpretation of Wang *et al.* [34, 35].

In addition to these experimental results, the evidence that the large Joule heating may not be beneficial for enhancing the emission power was also pointed out by the work of Tsujimoto *et al.* [43]. They fabricated their mesa device with separated two electrode terminals as shown in Fig. 17(a) in order to bias the dc-current from an electrode (on one side non-uniform bias) or from both electrodes (uniform bias). Additionally, they measured the mesa temperature directly using a Eu photoluminescent technique similar to the technique as described above [39, 40]. Figures 17 (b1) and 17(b2) show the temperature distribution images for the nonuniform-bias (b1) and uniform-bias (b2) cases. As shown in Fig. 17(b1) and 17(b2), we can easily find that the area of the hot spot seen in Fig. 17 (b2) is twice larger than that seen in Fig. 17(b1) and the local temperature of Fig. 17(b2) is higher than that of Fig. 17(b1). Now, by the comparison between these emission intensities, they found a correlation with the area

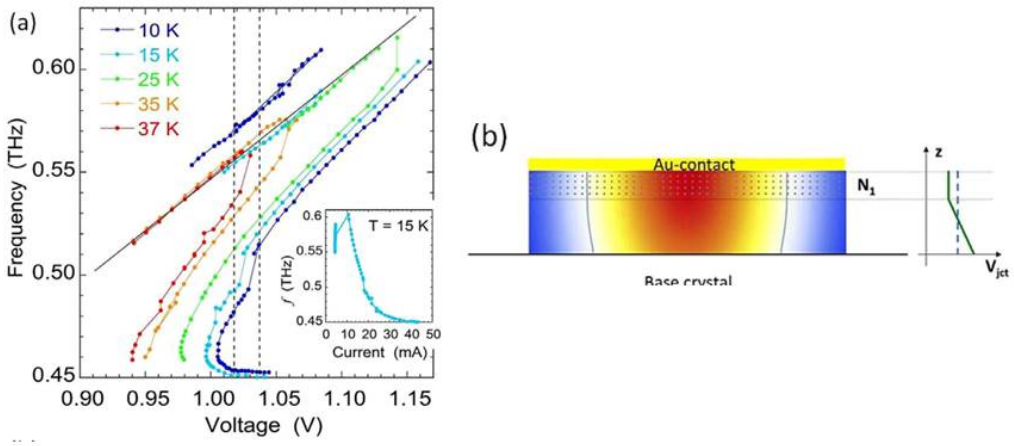

Fig. 18 The emission frequency f *vs.* biased voltage V and the image of the temperature gradient along the c-axis direction [45].

of the superconducting regions from which THz radiation is thought to have been emitted. As seen in Fig. 17(c), the evidence that the emission intensity with non-uniform bias feeding (less Joule heating, having a smaller hot-spot size) is higher than that seen with uniform bias feeding (large Joule heating, having a larger hot-spot size)is shown.

Next, let us consider the heating effect on the emission frequency. Benseman *et al.* carried out the simultaneous measurement of the emission frequency and the temperature distribution of a rectangular mesa device using a Eu photoluminescence technique [45]. They obtained the surprising experimental results shown in Fig. 18. It is the experimental observation that the measured emission frequency becomes significantly lower than the ac-Josephson frequency calculated by the biased voltage when the hot spot appeared in higher bias current region and the local mesa temperature exceeds the critical temperature, $T_{\rm c}$. They attributed such a deviation of the emission frequency from the ac-Josephson effect to the inhomogeneous temperature gradient appearing along the c-axis direction in the hot spot as displayed in an example of the numerical simulation in Fig. 18(b).

In contrast to this, Tsujimoto *et al.* detected the emission frequency in both the outer branch and inner multi-branches detailed in an earlier work [46] and they concluded that all the data points follow the ac-Josephson relation over the wide bath temperature, $T_{\rm b}$, range, not only in the outer-most branches but also in the inner branches. Considering all of the results presently available, we think that the possibility of the gradient of the voltage along the length of the rectangular mesa device may be more likely and significant than a voltage

gradient along the c-axis.

Part II

Motivation of the study

5.4 Motivation

In section 5, we saw that mesa devices temperatures below $\simeq 50$ K have serious Joule heating effect, which usually cause a hot spot and often influence the emission character of the mesa significantly. As noted above, there have been unclear arguments and debates, some of which even contradicted our understanding, and provided us with an insufficient explanation of the experimental results we have obtained. Therefore, we decided to investigate such problems experimentally to improve our understanding, because we think that this is very important for the improvement of THz emission towards higher emission power and frequencies. The purpose of this thesis is to devote my effort to better understand the Joule heating effect on the THz emission phenomena by clarifying experimentally the inhomogeneous heating problem, especially, the role of the "hot spot" on the THz emission. We think by doing so that we can go one step further to open the door for new developments of our THz devices.

To directly measure the local temperature of the mesa device, we employ a new method we developed, using SiC micro-powders coated onto the mesa's top surface. By shining UV light, the SiC micro-powder absorbs it and emits photoluminescent(PL) light and the intensity of its blue component shows a strong temperature dependence between 15 K and 150 K. In addition, SiC micro-powders are inexpensive and technically easy to handle and to cover the device surface. SiC is not transparent at visible light frequencies so that there is no reflection of the laser beam from the mesa surface. Therefore, we have been able to measure a much clearer image of the mesa temperature directly by the PL technique with simultaneous emission frequency measurements by the FT-IR spectrometer [47, 48].

Before and after our attempt to measure the mesa temperature directly, there have been several similar attempts by other groups to do so using Eu photoluminescent techniques [28, 49]. However, their temperature images were not as clear and gave ill-defined hot-spot behaviors. Since the absorption coefficient of the Eu film is low, the surface structures of the mesa structure, such as metallic electrode as the terminals, give some reflections in the temperature images and interfere with the real temperature images, resulting in lower quality images.

On the other hand, the measurement technique we developed, gives excellent results for the measurement of the local temperature at the resolution as small as ~ 4 μm. In addition, we could study the THz emission properties at various thermal conditions provided by the temperature, T, and external heat added by a laser beam at the various points of IVCs, and we finally were able to investigate the heating behavior of the mesa (strong temperature

gradient, hot-spot formation, *etc.*) in relation to the THz emission intensity and frequency [50].

In order to understand the influence of the heating effect on the the emission character in detail, we further measured the electrical potential distribution in the *ab*-plane of the rectangular mesa while the mesa is actively radiating THz waves. We focused in particular on the emission frequency, which must be proportional to the voltage per single Josephson junction as long as the ac-Josephson effect works as the primary emission source. This was done especially because, as we mentioned in section 5.3, Benseman *et al.* reported that the emission frequency, f, seems not to obey the ac-Josephson relation [45]. Their interpretation of this phenomenon relies upon the assumption that the inhomogeneous heating of the mesa existed along the *c*-axis direction. We doubted this interpretation of their results, because the temperature gradient along the *c*-axis direction is very small as seen in Fig. 14(b) [38] and we thought that it should not lead to a significant effect upon the THz emission. We think that it is more important to understand clearly the origin of the deviation from the ac-Josephson effect by our independent measurement technique [51].

In the following, the experiment and the results concerning the Joule heating problem of the THz emitting mesa devices are described in detail. At the end, we summarize our results and provide some conclusions we believe could be beneficial for further developments of the THz devices as well as for their applications.

Part III

Experimental technique

6 Sample preparation and development of the PL temperature measurement technique

All the Bi2212 single crystals used in this study were grown by a traveling-solvent floating-zone (TSFZ) method using an in-house modified-infrared-image furnace [52]. A piece of the Bi2212 single crystal was annealed at 600 °C over 48 hours in Ar + 0.1 % O_2 atomosphere in order to bring the sample to the slightly under-doped phase region.

The sample mesa device preparation technique is as follows:

i) After the crystal was glued onto a sapphire substrate by polyimide (PIX), it was cleaved to obtain a fresh surface.
ii) Then, Ag and Au layers were immediately deposited.
iii) and iv) The crystal was milled by the Ar ion milling method using appropriate metal masks.
iv)The sample surface was coated by oil-based paint.
v) After that, the oil-based paint was removed by acetone to eliminate the debris on the sample. The final dimensions of the mesa device were measured by Atomic Force Microscopy (AFM) and are about 80 μm in width, 400 μm in length and 2 μm in thickness.
vi) In order to apply the bias voltage along the c-axis direction, polyimide and CaF_2 were deposited to avoid current leaking. An example of an optical image of the mesa sample is shown in Fig. 19.
vii) Finally, a current lead (Au film) was attached to the top of the mesa by depositing Au and electrical leads were connected by Ag paint.
viii) The mesa surface was covered by the SiC micro-powders.

These sample preparation procedures are illustrated in Fig. 19 in detail.

In the course of this study, the SiC micro-powder was covered by hand on the device surface to measure the mesa temperature directly as shown in Fig. 19(viii) [47]. For the direct temperature measurement of the device surface and the emission frequency, we constructed an experimental set-up as shown in Fig. 20 (a). The sample was attached onto the Cu cold finger in a He-flow cryostat (Oxford instruments, CF1104). The emission spectra were measured by the FT-IR spectrometer (FARIS-1, JASCO, spectral resolution: k=0.06 cm^{-1}) at the angle of 70° tilted from the direction perpendicular to the sample. UV light from a

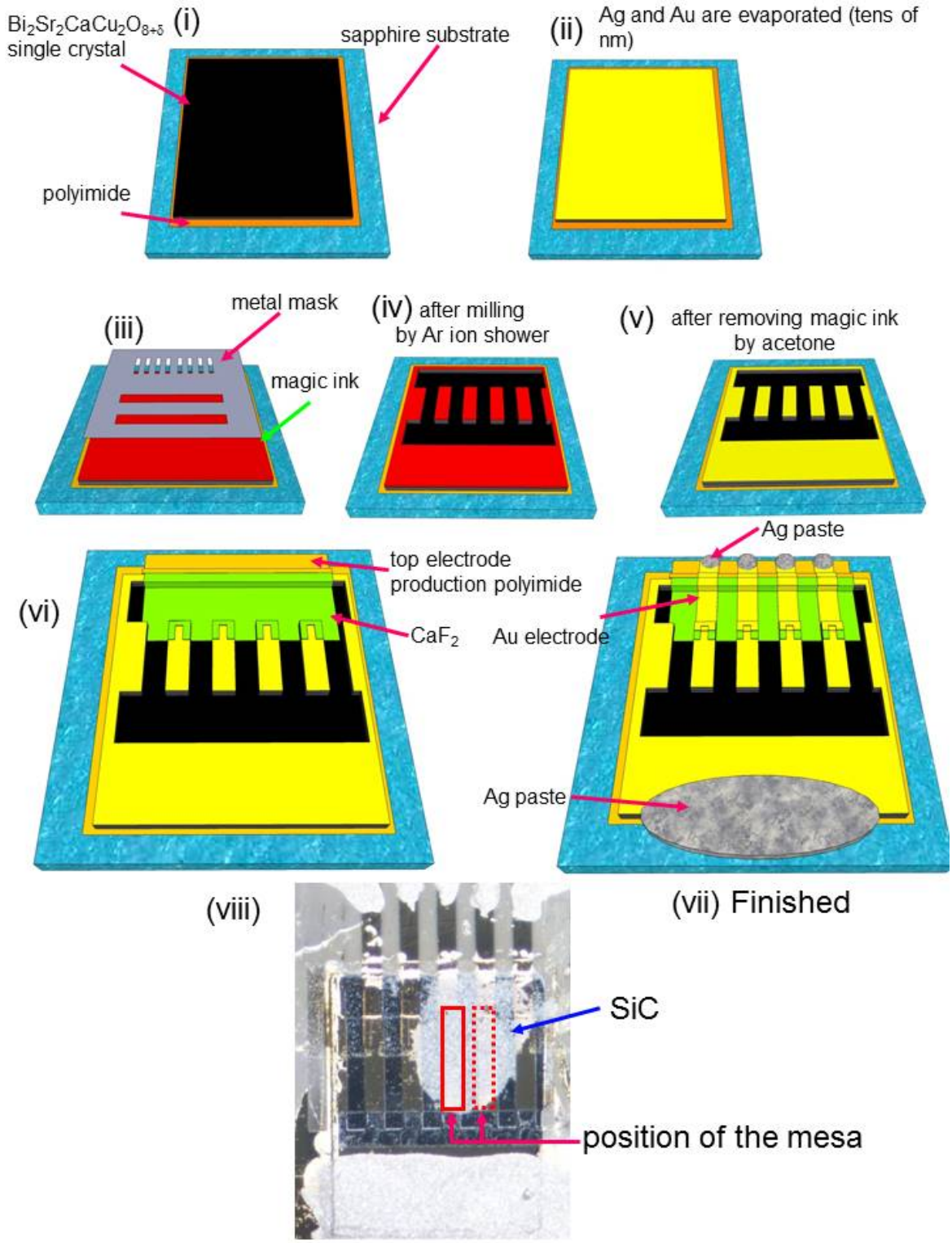

Fig. 19 The sample preparation method

commercial UV-LED lamp was uniformly shone onto the mesa surface at an angle of 25° from the normal to excite the SiC micro-powder indicator. The PL light from SiC micro powder was recorded by a CCD camera at the angle of 15° from the normal. Figure 20(b) is a photograph of SiC (gray area) on the Bi2212 mesa device. When the SiC is irradiated with the UV light, it emits photoluminescence of visible light as shown in Fig. 20(c).

Here, we describe the temperature calibration technique. In order to calibrate the SiC PL intensities with temperature, T , their integrated red, green, and blue visible light components were separately measured between $T_{\rm b}$= 15 K and 140 (150) K in steps of 5 K without any bias current I. The resolution of the photos as indicated in Fig. 20(c) is 1280 x 1024 pixels and each of them in the images contain the detected PL intensity of each of the three primary colors with 8-bit resolution. Since the blue component of the PL light has the strongest temperature dependence, the blue component of the light was selected to use for the temperature measurements. After the PL intensity was calibrated as a function of temperature between 15 K and 140 (150) K in each pixel, for every samples, the temperature distribution measurements were performed at various bath temperatures, $T_{\rm b}$, while the mesa is active with the dc-current applied to the mesa sample. We took the PL images under the same UV irradiation conditions, and the blue components of the accumulated images were compared with those of the images taken under emitting THz radiation at each pixel of the corresponding position one by one to determine the local temperature $T(r)$ map of the biased mesa. The overall spatial resolution of the $T(r)$ images was found to be about $3 \sim 4$ μm, depending upon the particle size of the SiC micro fine powder (μm scale).

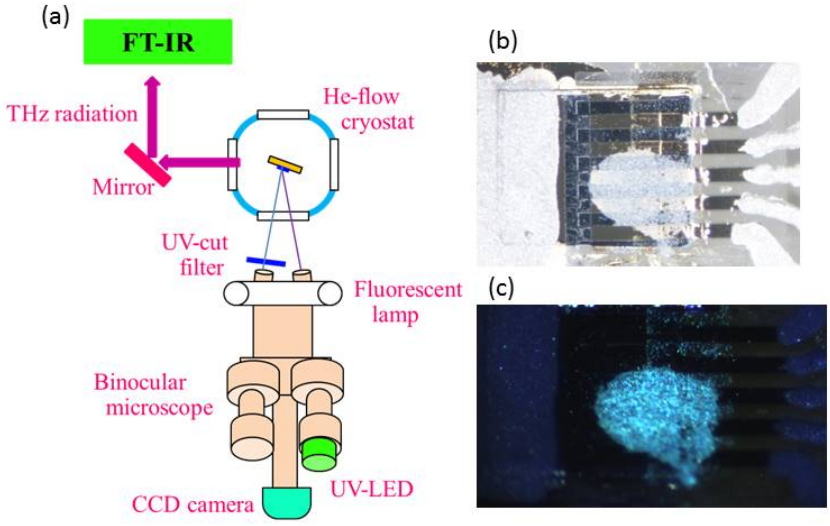

Fig. 20 (a) The sketched experimental set up for the simultaneous measurements of emission spectra and temperature distributions. (b)and (c) are optical images of the device.

Part IV

Experimental Results and Discussion

7 Simultaneous observation of the temperature distribution and THz radiation

7.1 Results

Here we show an example of a direct and simultaneous measurement of the local temperature of the mesa and THz emission using the SiC photoluminescence method developed by us as explained in Fig. 20(a). The dimension of the mesa is 79 μm in upper width, 89 μm in lower width and 2.4 μm in thickness. As shown in Fig. 21(d), clear temperature distribution images including sharp images of the hot-spot can be observed with high spatial resolution.

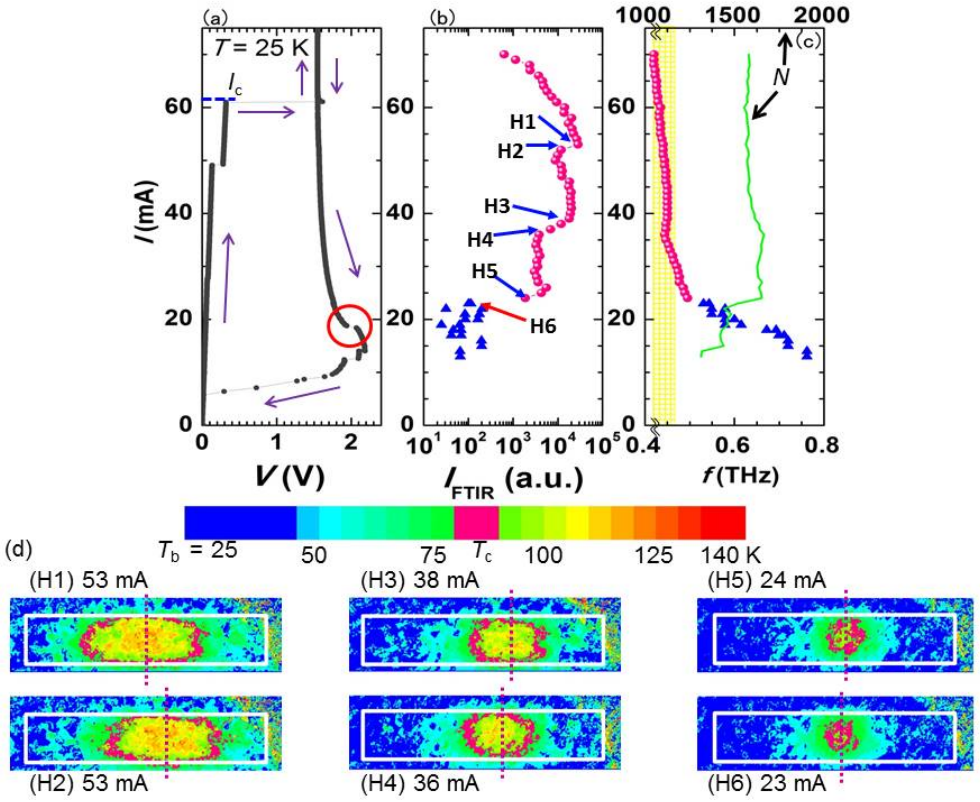

Fig. 21 (a) IVC at $T_b = 25$ K. (b) and (c) are the emission intensity I_{FTIR} and frequency f as a function of the current I. The green line in Fig. 21(c) indicates the number of Josephson junctions, N, calculated by the ac-Josephson effect. (d) The images of the local mesa temperature, $T(r)$, distribution.

In Fig. 21(a), the IVCs measured in the current bias mode are presented. After the bias current, I, exceeds the critical current, $I_{\rm c}$, of about 61 mA, the voltage appears correspondingly. It shows a typical negative differential resistance behavior due to self-Joule heating at the higher current regime and a large hysteresis loop due to non-linearity of the Josephson junctions at the former current regime while the current is swept up and down. In Figs. 21(b) and 21(c), we plotted the emission intensity, $I_{\rm FTIR}$, on a logarithmic scale and the frequency, f, measured both by FT-IR as a function of the current. As seen in these figures, this particular device emits relatively strong THz radiation in the wide current range between 70 mA and 10 mA. The yellow hatched area in Fig. 21(c) indicates a resonance frequency range corresponding to $420 \sim 480$ GHz assuming the half wave-length of standing wave in the width direction of the rectangular mesa allowing the width range from 79 μm to 89 μm. It is calculated by taking the trapezoidal shape of the mesa into account derived from the result of AFM measurement of the mesa size as 79 μm in upper width, and 89 μm in lower width. Note that, in both figures, when the emission spectra are separated into several peaks in the low current region, the symbols are indicated by blue triangles. As shown in Figs. 21 (b) and 21(c), the emission intensity dropped down suddenly and the emission spectra split into two as soon as f deviates from the resonance frequency at the current level indicated by H6. This result strongly suggests that the cavity resonance mechanism is working properly and efficiently to enhance the emission intensity in this region.

The local temperature, $T(r)$, images of the mesa obtained at 25 K at various current levels indicated by the points from H1 to H6 in Fig. 21(b), are indicated in Fig. 21(d). The white solid rectangles in Fig. 21(d) indicate the position of the mesa and the vertical red dotted lines represent the center positions of the hot-spot. We clearly found that the local temperature, $T(r)$, at the hot-spot region exceeds the $T_{\rm c}$. As seen in Fig. 21(d), the boundary between the hot-spot ($T(r) > T_{\rm c}$) and the superconducting surrounding region ($T(r) < T_{\rm c}$) is very sharp, so that the mesa is sharply divided into two regions: a superconducting and a normal conducting region. It is interesting to note that the strong THz radiation is emitted even in such a complicated heated condition in a higher bias current. This is rather surprising because both superconducting and normal states coexist at the same time in the same mesa while THz radiation is emitted.

We point out that the THz emission intensity, $I_{\rm FTIR}$, is not monotonic, sometimes suddenly jumps up(down) by almost an order of magnitude, as seen between points H1 and H2, and, H3 and H4 with in small current change and continuous change of IVC, although the emission frequency, f, continuous without discrete jumps within the cavity resonance frequency (yellow hatch) as shown in Figs. 21(b) and 21(c). We wonder why only the emission intensity jumps down (up) suddenly. After several measurements, we found an surprising explanation for this phenomenon. When the sudden jump of the emission intensity is observed, the position of the

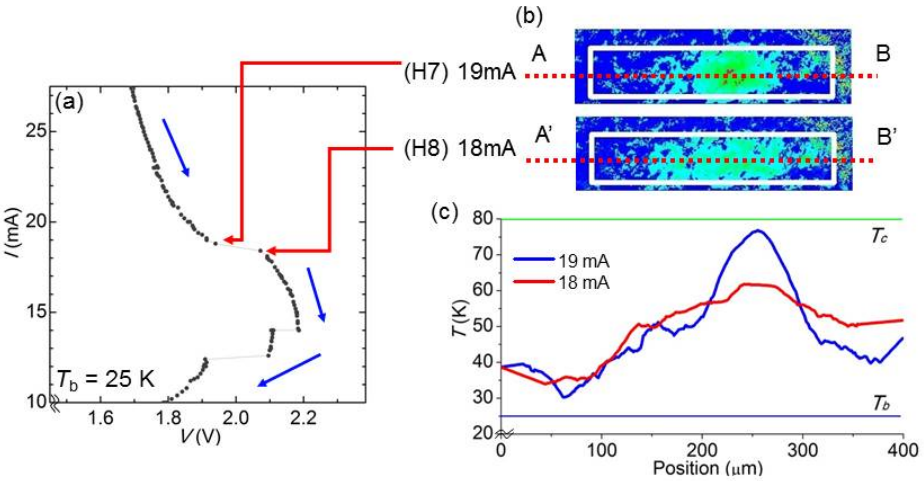

Fig. 22 (a)The enlarged figure of the IVCs around V: 2 V and I: 20 mA where is pointed by red solid circle in Fig. 21(a). (b) and (c) are the temperature image and the profile along the dotted line AB and A'B' in Fig. 22(b).

hot spot suddenly jumps to a new position as shown in Fig. 21(d). In comparing H1 with H2, and H3 with H4 for example, we easily recognize that the position of the hot spot also jumps to the right from H1 to H2, and to the left from H3 to H4. We attribute this peculiar sudden jump of the emission power to the sudden shift of the hot-spot position. Since this phenomenon occurs in the mesa while decreasing and increasing current reversibly, this strongly suggests that the change of the hot-spot position may enhance the emission intensity drastically if the hot-spot position is optimized. This may mean that not only the hot-spot formation itself, but also the shape and the position of the hot spot in the mesa probably strongly influences the radiation intensity.

On the other hand, in comparison between H5 and H6, the motion of the hot spot can hardly be seen, although the emission intensity is drastically decreased at H6. This fact may be very important because even though the intensity of the THz emission changes drastically, the hot-spot position and the emission frequency seem to be unchanged at all in this particular case. It is apparent that this surprising experimental result contradicts the previous study proposed by Wang *et al.* [34, 35]. We think that their experimental results may be misinterpreted as discussed in section 5.1.

As the bias current becomes lower, a sudden jump in the IVC is clearly seen. This is pointed out by the red solid circle in Fig. 21(a). We replot it in Fig. 22(a) on an expanded scale. The $T(r)$ images and temperature profile along the dotted lines corresponding to AB and A'B'

before (H7) and after (H8) the jump of the IVC are shown in Figs. 22(b) and 22(c). These figures clearly show that the hot spot suddenly and completely disappears at H8, although as seen in Figs. 22 (b) and 22(c), $T(r)$ is below T_c everywhere in both cases of images H7 and H8. It is noticed that the local temperature has a rather sharp peak in the case of H7, while it is rather flat everywhere in the mesa in the case of H8. This means that the hot spot is suddenly growing as the current is increases even by just 1 mA, suggesting that the jump of the voltage seen in between H7 and H8 may be caused by a sudden growth of the hot spot in the mesa. Note that the voltage in the higher current side (H7) is lower than the lower current side (H8) in the IVC. This clearly indicates that the hot spot works as a shunt resistor. The emission intensity as shown in Fig. 21(b) and 21(c) is weak in this region and does not show significant difference before and after the IVC jump. The hot-spot formation begins to occur and suddenly grows in somewhere in the mesa as soon as $T(r)$ exceeds the threshold temperature of $\sim$ 60 K. This is in good correspondence with the fact that the negative slope of the c-axis resistivity becomes significant below $\sim$ 60 K [38]. Therefore, the hot spot emerges suddenly from a rather homogeneous and wide-spread temperature distribution (H8) below $\sim$60 K as if an active volcano were erupting. This means that above 60 K there will be no hot spot at any current level. This is also confirmed in our measurements above 60 K [47, 48].

7.2 Conclusion

We studied the local temperature distribution, $T(r)$, in the mesa by SiC micro-powder PL measurements at various bath temperatures, T_b. At T_b=25 K, the relatively strong THz radiation was observed even under the severely inhomogeneous temperature distribution with the hot spot in the mesa. We first reconfirmed the experimental fact that the cavity resonance enhancement mechanism works properly and correctly at the half wave-length matched with the width of the mesa by measuring the emission frequency, f, by the FT-IR spectrometer. Because of that the emission intensity was dramatically decreased as soon as the emission frequency, f, deviated from the resonance frequency of the cavity. However, we could not find any positive piece of evidence that the hot spot could help the THz emission intensity. Therefore, we concluded that there is only the negative influence for the THz emission intensity but no evidence of a positive effect on the THz emission. This conclusion apparently contradicts the previous studies by Wang and others [34, 35].

Furthermore, we found a very interesting fact that the emission intensity suddenly jumps up and down reversibly when the hot spot moves along the long length by even a few micro meters. It seems that the emission intensity is very sensitive to the position of the hot spot. This is very surprising and is very curious to ask a question what causes such a sharp difference in the emission intensity in the single crystalline material of the mesa. Although we do not have

an appropriate answer to the question at the moment, this phenomenon could be understood as a case of self-organization in that the system in the nonequilibrium state tries to find itself in the most stable state (or quasi-stable state). This can be interpreted as a self-impedance-matching (or self organization) phenomenon for the THz radiation. It is also very interesting to point out that such a phenomenon, in turn, can be viewed from a different point. Since the THz emission intensity can be varied by changing the position of the hot spot, it may be possible even to control the emission intensity by controlling the position of the hot spot artificially by some means.

Secondly, as for the THz radiation frequency, it changes continuously without noticeable jump although the intensity jumps up and down at a certain current level in response to the sudden shift of the hot spot's lateral position in the mesa. This observation contradicts the previous study that the size and the position of the hot spot tunes the emission frequency, f, [34, 35], which is determined by the rest of the superconducting part of mesa being in resonance with the emission frequency along the length direction. According to the study of Wang *et al.*, the larger hot spot in the mesa would generate a higher radiation frequency. However, in our case as seen in Fig. 21(c), the higher current (corresponding to the larger hot spot) makes a shift to lower emission frequency. The our result shows totally opposite behavior and, therefore, completely conflicts with the statement given by Wang *et al.* [34, 35].

Finally, we note that the correlation between the disappearance of the hot spot and the jump of the IVC. This sudden jump in the voltage is well understood by a sudden formation of the short cut in the current path along the c-axis direction of the mesa structure due to the formation of the hot spot, where the local resistance becomes much lower than the other part of the mesa. This instability occurs spontaneously and locally by breaking the uniformity of the system (*i.e.* constant temperature everywhere of the sample before the hot-spot formation) and making it very inhomogeneous locally by itself. Once the hot spot forms in the system, the rest of the system is left nearly unchanged.

Although the emission frequency, f, starts to increase due to the increase of V as the current is reduced through the voltage jump, the emission power is always low at this region and hardly differs before and after the V jump. Although we admit that the hot spot affects the THz emission very intimately, and it sometimes seems to correlate strongly with the emission intensity as discussed above, we conclude that the hot spot is certainly not the crucial mechanism for the THz emission but it always gives a cumbersome effect or severe suppression effect on the THz emission.

8 Influence of the local heating by an external laser beam on the emission intensity

8.1 Experimental set-up and procedure

In the former section 8, we found a sudden improvement of the emission intensity when a hot spot moves to an appropriate position along the long length direction. From this observation, we came to the conjecture that the emission intensity may drastically be improved by manipulating and adjusting the local position of the hot spot in the mesa structure. In order to control the position of the hot spot, we introduced a laser beam as an additional heat source, making it virtually similar to the hot spot, which can finely be focused on the mesa to heat it locally. The experimental set-up for this purpose is schematically shown in Fig. 23, where the detailed mesa structure and its surroundings are schematically shown in Fig. 23(a), and the experimental set-up is illustrated in Fig. 23(b). Because the temperature dependence of the c-axis resistance in Bi2212 single crystal is semiconducting-like at low temperatures, the c-axis current tends to concentrate in the hotter region because the hotter part of the mesa has a lower resistance than the other colder part. This causes a catastrophic instability of the heating condition resulting in the further development of the inhomogeneous temperature distribution in the mesa by itself. As a result, the drastic change of the c-axis current distribution is expected, when the external heated area by the laser beam goes beyond $T_{\rm c}$.

In the experimental set-up for this measurement shown in Fig. 23(b), a mechanism to control the hot-spot position with an external laser beam is added. Here, we used a blue laser with a wave length of 405 nm, having a maximum power of about 80 mW, which is sufficient to bring the sample local temperature, $T(r)$, well above $T_{\rm c}$. The laser was attached to an external manipulator as shown in Fig. 23(b) and the laser spot was focused within the width of the mesa. Since the beam size is about 80 μm in diameter, the mesa with the width of 80 μm can be just covered by this laser beam. The experimental set-up to measure the mesa temperature, including the emission power, $I_{\rm FTIR}$, and the frequency, f measurement were the same as shown in Fig. 20(a). In this experiment, we used the same mesa device (sample #1) as shown in the section 8 in Figs. 21 and 22.

8.2 Results

First, we show the IVC (current-voltage curve) at $T_{\rm b}$=25 K under UV irradiation without laser heating in Fig 24(a). It behaves as a typical IVC with a significant back-bending behavior

due to the Joule self-heating effect. At the current indicated by the small red circle on the IVC in Figure 24(a), all of the experiments with laser heating were done. Figure 24(b) shows the direct images of the PL emission from SiC micro-powders recorded by the CCD camera. The red rectangles indicate the position of the mesa device, and the darker area is a hotter place (hot spot), which is indicated by yellow rectangles. The green dotted lines signify the center of the hot spot. As shown in the panel L1 in Fig. 24(b), a hot spot without laser irradiation is located close to the center position of the mesa. After introducing the laser beam indicated by the bright image of a white spot, we moved the laser beam position from the upper side (L2) to the lower side (L5) of the mesa. We found that the position of the hot spot is very sensitive to the position of the laser heating spot. When the mesa was heated at the upper side of the mesa device, the hot spot moves slightly up toward the laser beam position (L2) as if the hot spot were attracted by the laser beam spot. As the laser beam spot is further shifted down close to the hot spot, and overlaps with it, the hot spot moves down with it (L3 and L4) as if the hot spot were dragged by the laser beam. However, at panel L5 the hot spot returned to its original position away from the laser beam spot as shown in panel L1, probably because the laser beam moved too far away from the original hot-spot position

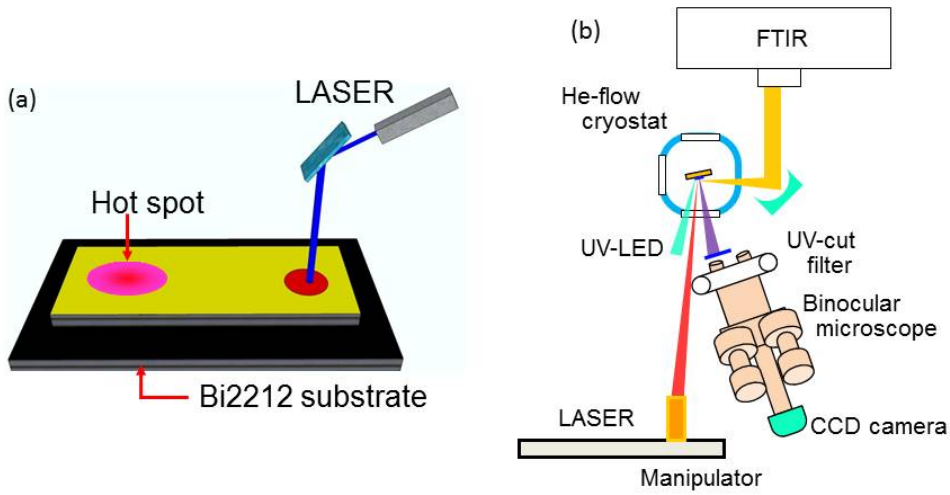

Fig. 23 (a) A schematic view of the mesa and external heating mechanism in order to adjust the hot-spot position. (b)The experimental set up for the simultaneous measurement of the local temperature and the emission character under the external heating by the focused laser beam.

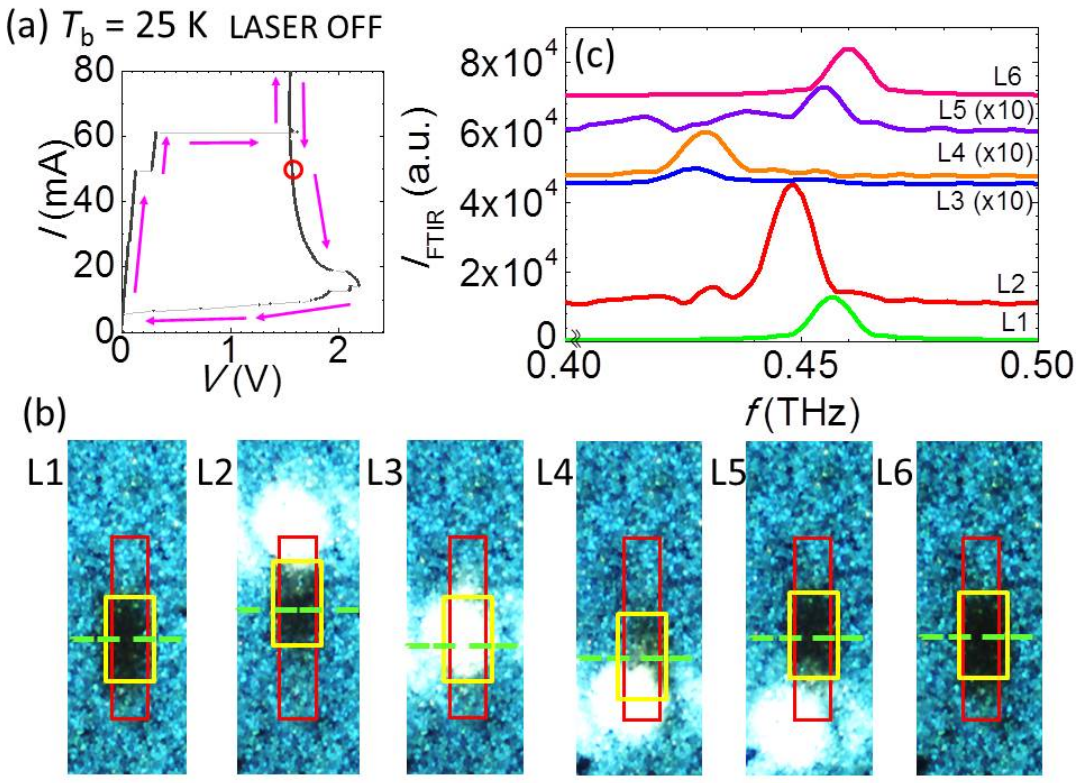

Fig. 24 (a)The IVC at T_b=25 K. (b) The photos of photo-luminescent light from SiC obtained directly from CCD camera. The mesa was heated by the focused laser beam (the bright spot in H2 $\sim$ H5). (c) The emission spectra at H1 $\sim$ H6 in (b).

(L1). Finally, when the laser beam was turned off at panel L6, the hot spot remains in the original position (L1).

At the same time, we measured the THz emission spectra while the image of the PL emission is recorded. Experimental results are presented in Fig. 24(c), where L1 to L6 on each spectrum have one-to-one correspondence with the panels from L1 to L6 in Fig. 24(b). The remarkable points observed here are that the THz radiation intensity varies strongly depending on the hot-spot position. The THz emission intensity becomes much larger in L2 than those in all other spectra of Fig. 24(c). On the other hand, when the laser beam position is at the center or lower position (L3 to L5), the emission intensity becomes much weaker than that without the laser beam (L1 and L6). Here, it is surprising that all the emission spectra fulfill the cavity resonance frequency (420 $\sim$ 480 GHz). It is clear that this result can exclude completely such a possibility as claimed by Wang *et al.* [34, 35] that the result of the superconducting part along the length direction of the mesa has a standing wave resonant mode and emitting THz wave in accordance with the length of the superconducting part of the mesa. Although it is not clear at this moment why the emission intensity is improved when the hot-spot position

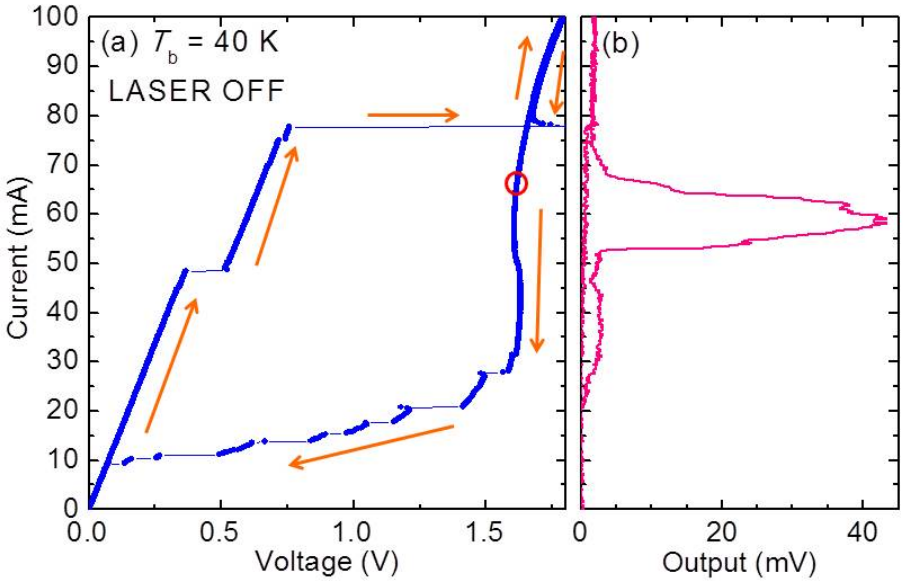

Fig. 25 (a)The IVC at $T_{\rm b}$= 40 K without laser heating. (b) The emission intensity measured by hot-electron bolometer as a function of the current, I.

is driven towards the top of the mesa or perhaps it comes near to the current injection point (the panel L2 in Fig. 3(d)), it is speculated that there may be a more suitable position for the hot spot to have stronger intensity of the emission [50]. In the panel L3 in Fig. 24(b), when the hot spot separates the mesa into two superconducting regions, it appears to have the weakest intensity. It is difficult to understand clearly why the emission intensity is greatly different between L2 and L4.

In order to understand more deeply the mechanism of the THz emission with the hot spot and to confirm the reproducibility of the increase of the intensity by controlling the heating condition in detail, another mesa device, sample #2, was fabricated. Sample #2 is 80 μm in width, 400 μm in length and 2 μm in thickness. In this experiment, we used the same experimental set-up shown in Fig. 23(b) and the emission intensity was detected by the hot-electron bolometer. We used a red laser instead of the blue laser for the additional heat source. Since the SiC PL light shows the strongest temperature dependence for blue color, both the SiC PL light and blue laser light were detected by the CCD camera indistinguishably. Therefore, in the former measurements we could not make temperature distribution images of the mesa under the irradiation of the blue laser as seen in Fig. 24(b), where the figures are not converted to temperature maps but they are the raw images from the CCD camera. On the other hand, since the red laser light is not directly detected by the CCD camera because

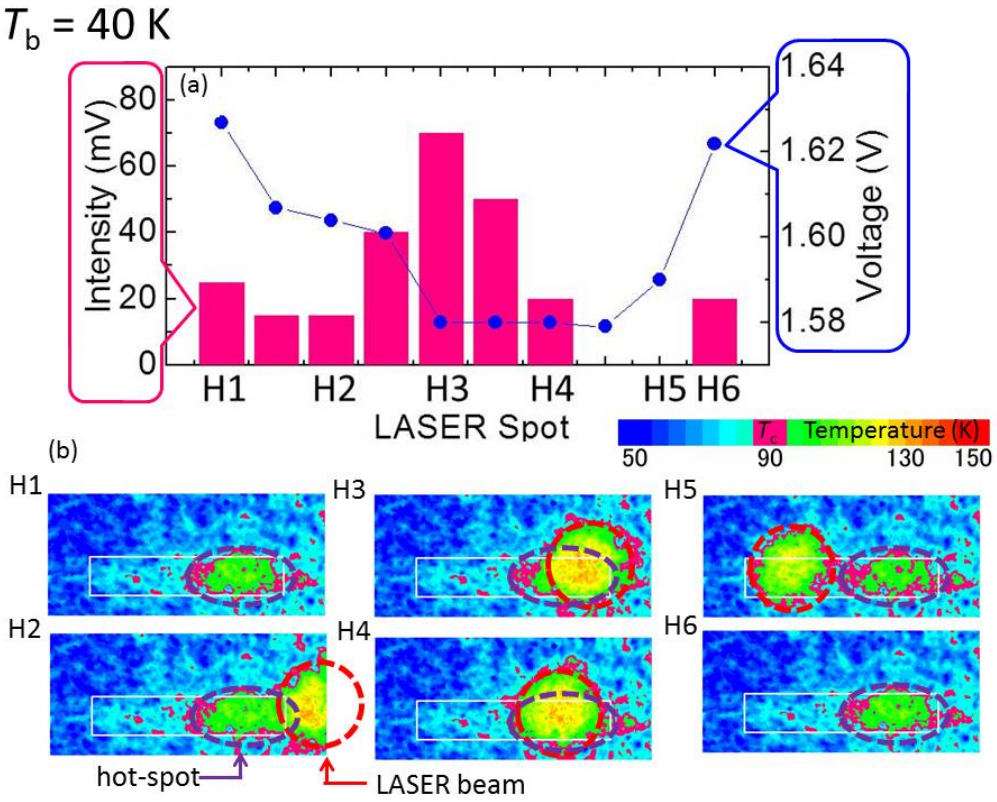

Fig. 26 (a) The emission intensity (pink histogram) and the measured V at H1 $\sim$ H6 which have one-to-one corresponding to them in (b). (b) The $T(r)$ images of the sample #2 at $T_{\rm b}$=40 K and I=65 mA. The red and purple dotted circles indicate the position of the laser beam heating and hot-spot position, respectively.

of its different color, we could make $T(r)$ images from sample #2.

The IVC of sample #2 at 40 K is presented in Fig. 25(a) and the THz radiation detected is shown in Fig. 25(b) by the hot-electron bolometer without laser irradiation. In this measurement, we observed relatively strong THz radiation in the higher bias current region where the hot spot absolutely exists. In Fig. 26(b), the $T(r)$ images of sample #2 are shown with the color code at $T_{\rm b}$ =40 K and I=65 mA, where the red solid circle is marked in Fig. 25(a). Here, we note that the current was always injected from the right-hand side of the mesa. The white rectangles, and the red dotted circles in Fig. 26(b) indicate the mesa position and the position of red laser beam, respectively. When the red laser beam was turned off, the hot-spot which is highlighted by the purple dotted circle, appears near to the current injection point at the right hand side of sample #2 as seen in H1 in Fig, 26(b). This sometimes happens because of the extra heating due to excess contact resistance at the current injection point.

As seen in panel H2 in Fig. 26(b), the temperature at the laser heating position exceeds $T_{\rm c}$. The laser beam was scanned from the right to the left hand side of the mesa surface (H2 $\sim$

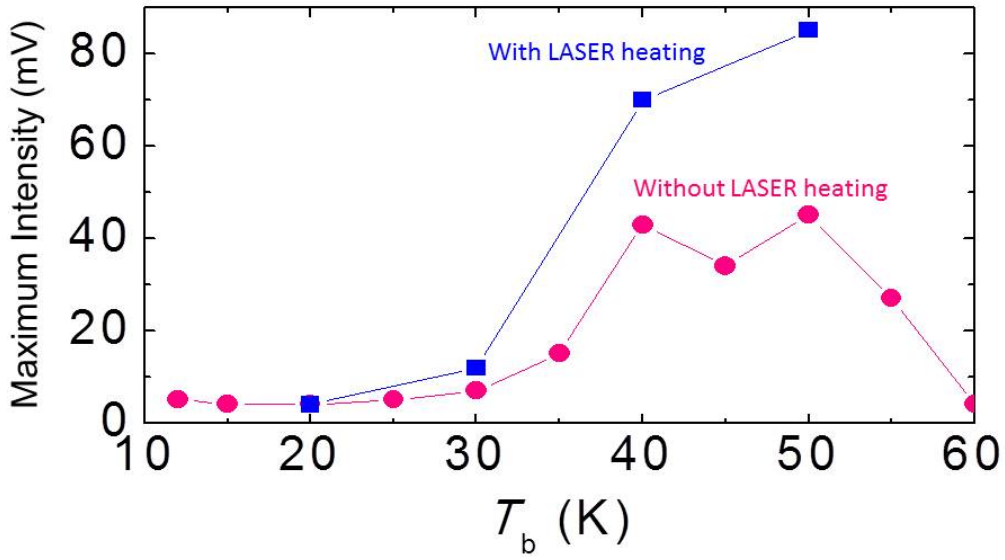

Fig. 27 The maximum emission intensity with laser heating (blue symbols) and without laser heating (pink symbols) *vs.* the bath temperature, T_b. The emission power was drastically enhanced by external heating.

H5). However, the hot spot did not move at all in this case. Figure 26(a) shows the emission intensity detected by the hot-electron bolometer by the pink histograms observed at the angle of 20 ° tilted from the sample surface, and the voltage observed at the I injection point (the blue dots). Although the hot-spot position keeps its original position, it is surprising that the emission intensity is drastically increased at panel H3 and is three times larger than that at panel H1 in Fig. 26(a). However, when the laser spot moved slightly from panel H3 to the new position in panel H4, the emission intensity suddenly decreased to as small as that at H1 in Fig. 26(a). Nevertheless, the voltage does not change between H3 and H4. Eventually, the emission intensity becomes zero at H5 (see Fig. 26(a)) when almost the entire mesa has $T(r)$ exceeding T_c as seen in panel H5 of Fig. 26(b). Finally, when the laser beam was turned off at H6, both the $T(r)$ image and the emission intensity at H6 were restored to the same patterns as before laser irradiation, as shown in panel H1.

These results are consistent with those seen before in Figs. 24(b) and 24(c) and the reproducibility of the enhancement of the emission intensity by the laser heating was confirmed. Moreover, we found that this phenomenon was observed over the wide bath temperature, T_b range between 30 K and 50 K as shown in Fig. 27. In Fig. 27, the pink dots represent the maximum emission intensity when the mesa was not heated by the focused laser beam,

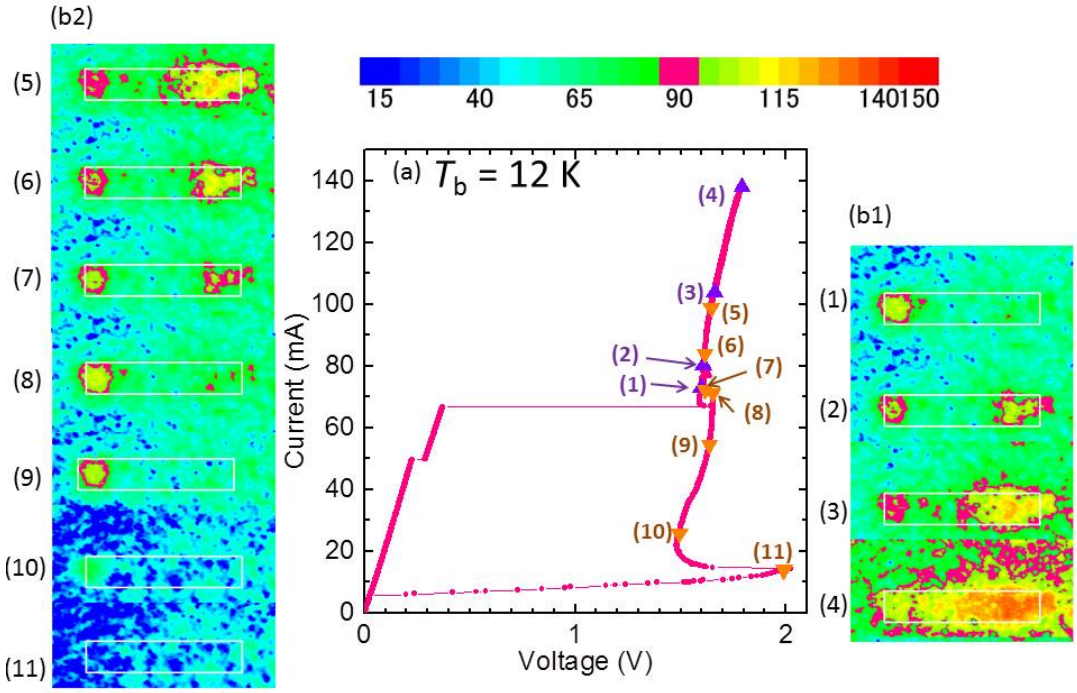

Fig. 28 (a)The IVC at $T_{\rm b}$= 12 K without laser heating. (b) The temperature images of sample #3 which has two hot-spots in the higher current region.

whereas the blue solid squares indicate that with laser heating. It is noted that the THz emission power with the laser beam becomes at least twice as large than that without the laser beam at 50 K when $T(r)$ is adjusted to get the maximum intensity. It is interesting to point out that such a drastic enhancement of the emission power could not be achieved if the mesa were not heated by the laser beam.

Up to here, we have shown successful enhancement of the radiation power by adjusting the local $T(r)$ using a laser beam. In order to reconfirm such results, we performed the same measurement using the other mesa device named sample #3, which has the characteristic features in the temperature distribution as shown in the temperature images (1) $\sim$ (11) of Figs. 28(b1) and 28(b2). The numbers in the Figs. 28(b1) and 28(b2) have one-to-one correspondence with the points in Fig. 28(a). The IVC of sample #3 at $T_{\rm b}$=12 K is presented in Fig. 28(a).

As soon as the current, I, exceeds the critical current, $I_{\rm c}$, the measured voltage, V, suddenly appears as indicated by the point (1) in Fig. 28(a). At the same time, the hot-spot appears at the left hand side of the mesa as shown in (1) in Fig. 28 (b1). Note that the current, I, is

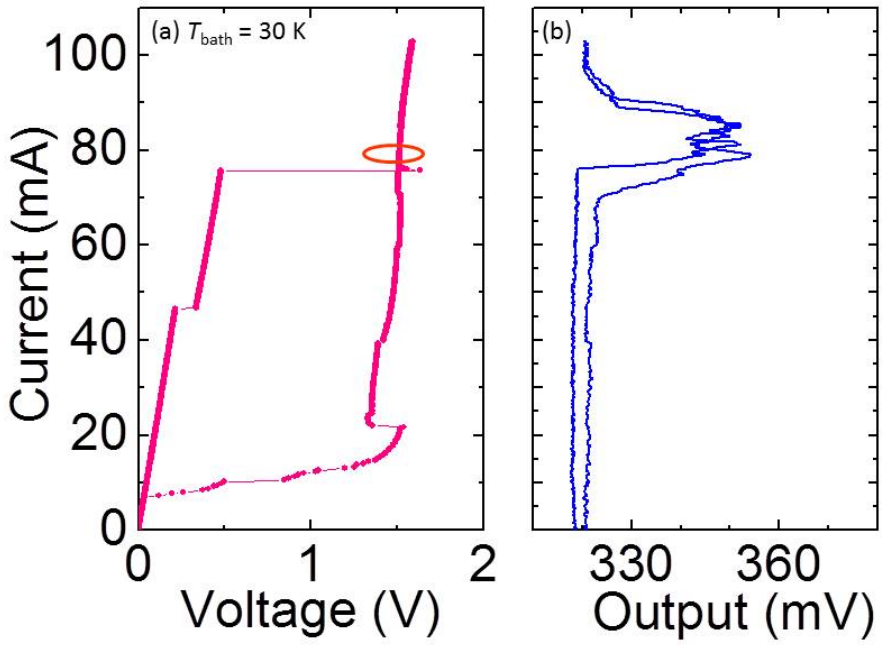

Fig. 29 (a)The IVC at $T_{\rm b}$= 30 K without laser heating. (b) The emission intensity, $I_{\rm bolometer}$, measured by the hot-electron bolometer as a function of the bias current, I.

injected from the edge of the right hand side of the sample #3. With increasing the current further, another hot spot begins to appear at the right hand side near to the current injection point. It is noted that the small hysteresis in the IVC can be seen between points (1) and (2) in Fig. 28(a). We noticed that the appearance of the second hot spot causes this small hysteresis in the IVC. As the current, I, is further increased, the hot-spot region at the right hand side only expands larger as shown in images (2) $\sim$ (4) in Fig. 28(b1), although the size of the left hand side hot spot is kept unchanged. When the current, I, is reversed from the highest point at (4) to the lower side in the IVC, the temperature distribution images are shown in (5), (6) and (7) in Fig. 28(b2). As the current is further reduced, the hot spot at the left side disappears at (11) of Fig. 28(b2). At the same time, as seen in Fig. 28(a) the voltage jumps up by about 0.5 V. This tendency is consistent with the experimental results of sample #1 as seen in Fig.22(a).

In contrast to sample #2, sample #3 has a peculiar two hot-spot behavior. We wondered whether or not the radiation intensity even in such a case could be controlled by the laser heating. We first show the IVC and the emission intensity measured by In-Sb hot-electron

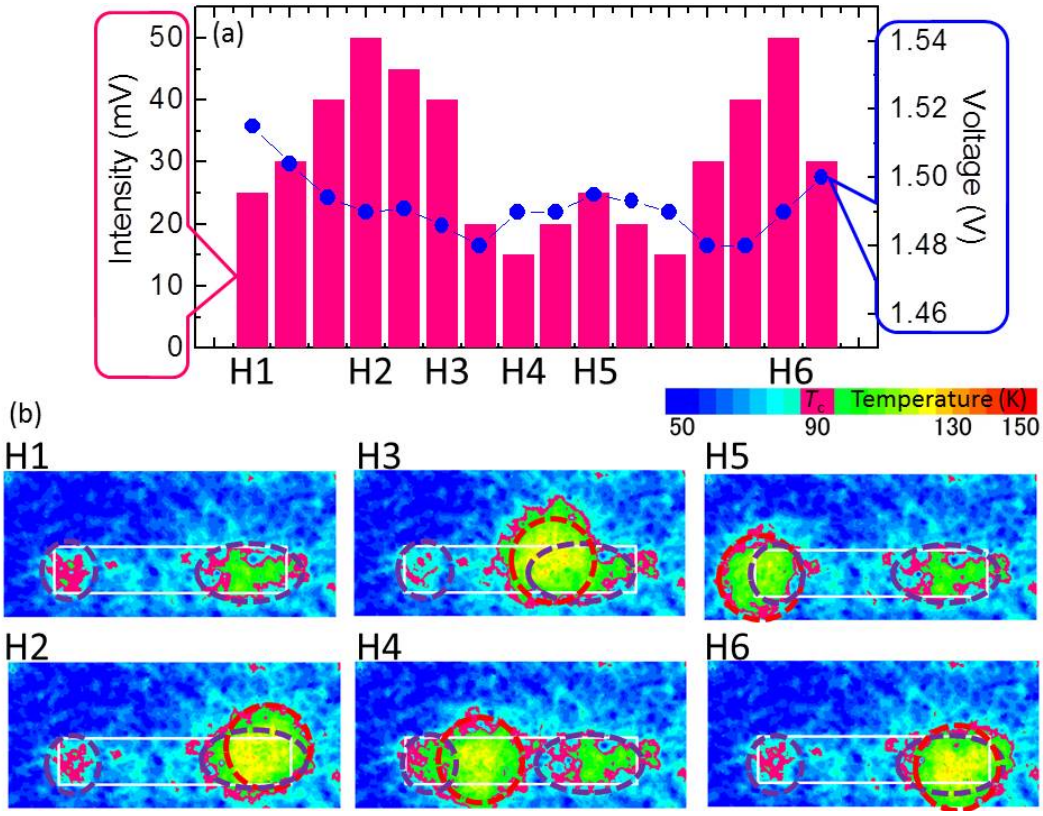

Fig. 30 (a)The emission intensity (pink histograms) and measured voltage (blue symbols) from H1 to H6. (b) The local temperature images of sample #3 from H1 to H6.

bolometer in Figs. 29(a) and 29(b) at T_b=30 K, respectively. As seen in Fig. 29 (b), the strong THz radiation can be observed in the high bias-current region of I= 90 $\sim$ 80 mA.

Then, we tried to control the heating condition using sample #3. The $T(r)$ images of sample #3 are presented in panels H1 to H6 of Fig. 30(b) at T_b=30 K and I=80 mA, which is obtained at the red solid circle position in the IVC as shown in Fig. 29(a). As indicated by the purple dotted circles, there are two hot spots without laser heating as shown in the panel H1 in Fig. 30(b). Then, the laser beam is focused on the mesa and scanned from right to left as shown from H2 to H5. During the laser scanning on the mesa surface from panels H2 to H5, the voltages of the mesa did not change significantly. However, when the sample was heated at the right hand side of the mesa, *i.e.*, the point near to the current injection point, the enhancement of the emission intensity was observed near H2 and H6 as seen in Fig. 30(a).

8.3 Conclusion

Concluding this section, we state confidently that the THz emission power can be enhanced further by manipulating and adjusting the heating condition using a focused laser beam as

an external heat source to control the hot spot. We have experimentally confirmed the enhancement of the radiation power from the mesa by at least a factor of two, although each individual three samples have three different emission characteristics as well as appearances of the hot spot. Although the mechanism of such a drastic improvement of the emission power is not understood well at this stage, we found the phenomenological tendency that the emission power becomes strongest whenever the position of the hot spot stays at or near to the current injection point of the mesa. This empirical finding can become more evident when the external heat source is added and the hot spot was dragged by the laser beam spot. Another point to be mentioned from our experimental observation lies in the postulation that the size of the superconducting area occupying in the mesa , which may also depend on the location and the size of the hot spot, *i.e.*, the size of the normal part of the mesa plays a very important role for the intense THz radiation, probably because the THz emission is generated from the superconducting parts of the mesa.

9 Electrical potential distribution in THz emitting rectangular mesa devices

9.1 Experimental set-up and sample preparation

In order to understand the influence of the heating on the emission character in more detail, we have also measured the electrical potential distribution in the *ab*-plane of the rectangular mesa device. As we pointed out before, Benseman *et al.* have measured the emission spectra and the temperature distribution of the rectangular mesa, and reported that the emission frequency, f, seems to violate the ac-Josephson relation. They interpreted this phenomenon by the temperature gradient effect along the *c*-axis direction caused by the inhomogeneous heating effect of the mesa along the *c*-axis direction [45].

However, in the previous experiment by Tsujimoto *et al.*, it was reported that the emission frequency follows the ac-Josephson effect not only in the outer-most branch but also the inner branches within the experimental error over the wide range of the bias current [46]. This result seems to contradict that of Benseman *et al.* [45].

We wondered what causes such a difference between two previous measurements. We hit on an idea that in a long rectangular mesa, the measured voltages at various positions along

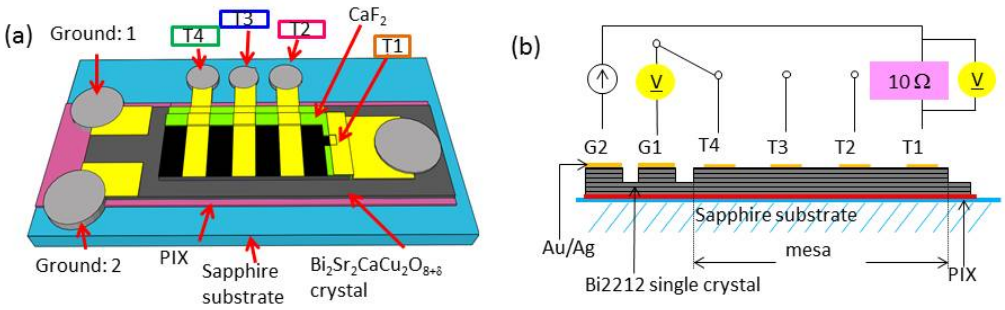

Fig. 31 (a)Schematic illustration of the mesa to measure the electrical potential distribution, $V(r)$, with four electrode terminals denoted T1, T2, T3 and T4. (b) The equivalent electric circuit representing the mesa shown in (a). The current was always injected from terminal T1.

the length direction may be different locally because the mesa is separated into two superconducting regions by the normal hot-spot region. We hypothesized that the voltage may not be equal at the top electrode from place to place if the current flows in the hot-spot region, where the c-axis resistance is lower due to higher temperature. So, we made a rectangular mesa device to measure the electrical potential distribution at the top electrode, the emission frequency and the temperature distribution of the top electrode simultaneously.

In order to measure the potential distribution of the top electrode, we fabricated a new mesa sample #A with the dimensions of 80 μm in width, 400 μm in length and 2 μm in thickness with four electrode terminals named T1, T2, T3 and T4 being attached along the long length. A sketch of this device is given in Fig. 31(a). In this experiment, the current was always injected from terminal T1 as shown in the equivalent electrical circuit diagram given in Fig. 31(b), and the voltage was measured at terminals T2, T3 and T4 by the four-probe technique.

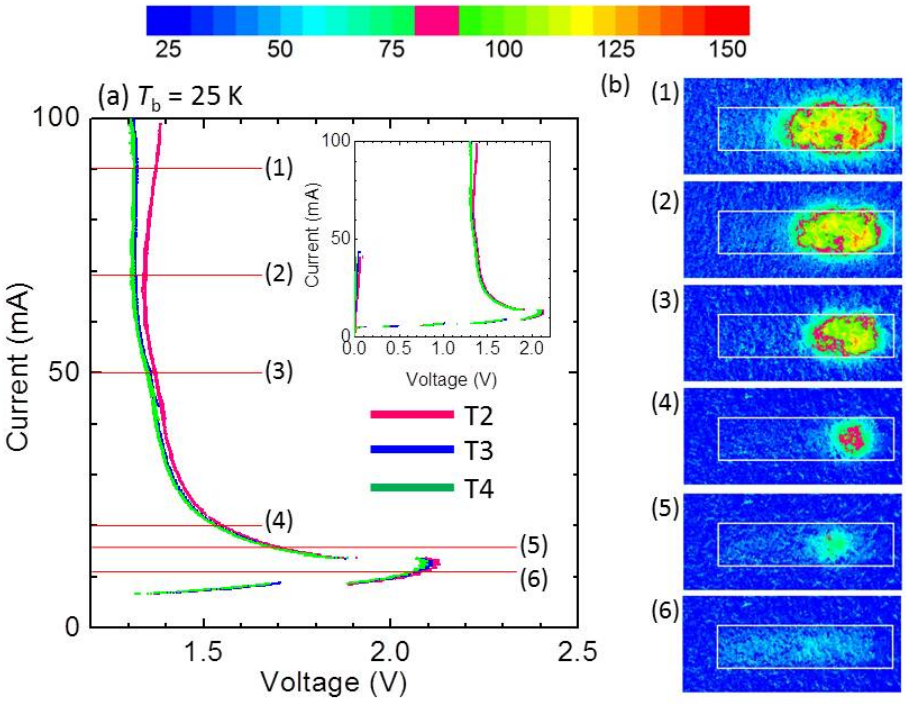

Fig. 32 (a) The IVC of mesa #A measured at T_b=25 K. This figure is cut from the whole IVC and enlarged by expanding the bias voltage axis, leaving the ordinate unchanged. The pink, blue and green lines indicate the IVC, where the voltage is measured at T2, T3 and T4 respectively. (b) The temperature distribution images of sample #A at various bias currents at the points indicated by numbers (1) to (6) in (a).

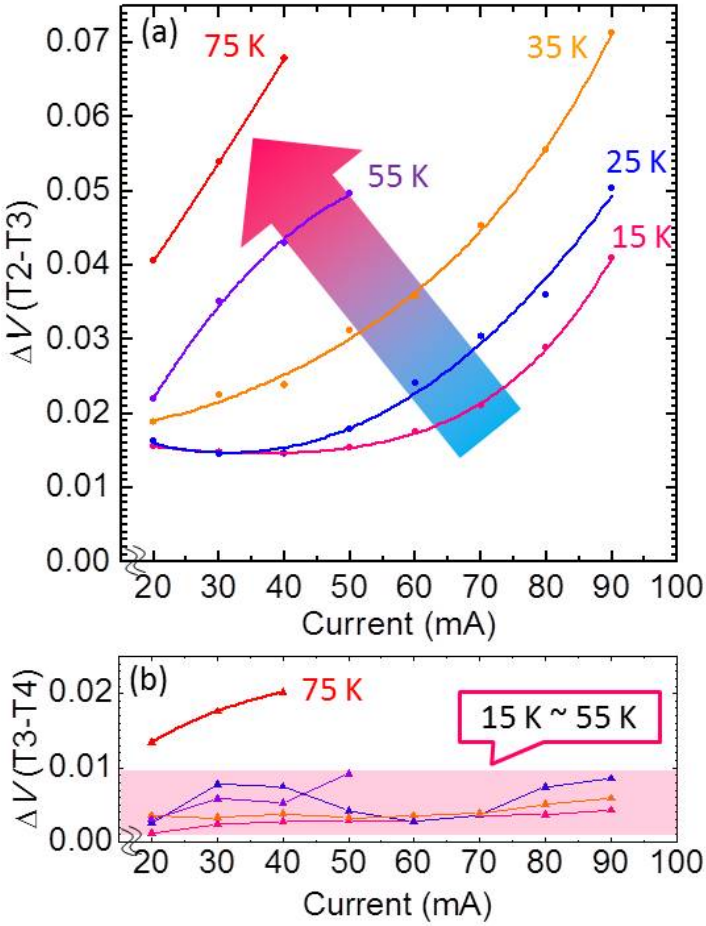

Fig. 33 (a) and (b) are the difference in the voltage measured between at terminal T2 and T3: $\Delta V(\mathrm{T2}-\mathrm{T3})$ and between at T3 and T4: $\Delta V(\mathrm{T2}-\mathrm{T3})$ *vs.* the bias current, I, at several bath temperatures.

9.2 Results

The results were very intriguing and remarkable. What is remarkable in the results, obtained in these measurements, is th there appears to be a large potential gradient when the hot spot is included in the current path along the length direction of the mesa. The inset of Fig. 32(a) represents the entire IVC at T_{b}= 25 K, whereas the main frame of Fig. 32(a) is cut out from the whole IVC shown in the inset of Fig. 32(a) and display only the higher bias voltage region. The pink, blue and green curves indicate the IVCs measured by the four-probe method, when the voltages relative to that at T1 are measured at electrode terminals T2, T3 and T4. As shown in Fig. 32(a), as the current, I, is increased, the local voltage $V(r)$ becomes inhomogeneous and the $V(r)$ at T2 becomes larger than that at T3 and T4.

In addition to the results of multi-terminal potential measurements, we show the local temperature distribution, $T(r)$, of sample #A measured by the PL technique in Fig. 32(b) from (1) to (6), which correspond to the current levels from (1) to (6) of the IVC in Fig. 32(a), respectively. In panel (5) in Fig. 32(b), the hot spot begins to appear between terminals T1 and T2 because of heating due to the contact resistance at terminal T1. As the current, I, is increased, the hot-spot size increases monotonically. It is noted that when the current, I, is increased gradually above I_c, the hot-spot size just grows gradually and $T(r)$ at T2 becomes higher than that at T3 and T4, leaving $T(r)$ at T3 and T4 is still lower than T_c. Corresponding to this $V(r)$ at T2 becomes higher than that at T3 and T4 accordingly. Therefore, the increase of the difference in the voltage, V, between T2 and, T3 and T4 corresponds to the growth of the hot-spot size as shown in Figs. 32(a) and 32(b).

Furthermore, we measured the voltage, V, at several bath temperatures and the results are shown in Fig. 33(a) and 33(b). Figure 33(a) represents the difference, ΔV(T2-T3), in the voltage between T2 and T3. In contrast to this, as seen here in Fig. 33(b), when the current, I, increases, the voltage difference, ΔV(T3-T4), between T3 and T4 is still zero below T_b =55 K. However, as T_b is increased, ΔV(T3-T4) eventually increases at T_b = 75 K, because the hot spot disappears and more or less a uniform temperature distribution appears at this temperature or above it. These experimental results strongly suggests that there is a noticeable potential difference along the long length direction of the rectangular mesa, as long as the hot spot is formed in the mesa.

Now, we can ask why such a large potential gradient exists in the mesa device. We attribute the appearance of such a large potential gradient along the *ab*-plane to the appearance of the normal conducting part due to the local heating (hot spot) where $T(r) > T_c$. This electrical potential distribution resulted from the experiments shown in Fig. 33(a) and 33(b) can be schematically illustrated in Figs. 34(a), 34(b) and 34(c), which present the side views of the mesa. When $T(r) < T_c$ is realised in the entire area of the mesa, the entire area is superconducting as seen in Fig. 34(a) and everywhere in the mesa along the *ab* direction is equipotential, resulting in the uniform potential everywhere. In such a case, since the superconducting current is confined within the top superconducting layer only because of the enormous anisotropy, the potentials of each layer are constant and equal within each layer. On the other hand, when the hot-spot ($T(r) > T_c$) exists in the mesa, it creates a local normal conducting region in the superconducting mesa and highly anisotropic resistive conduction shows up locally. Because of that, the current, I, flows inhomogeneously and the equipotential condition at the top surface region is lost as seen in Fig. 34 (b). For example, if the current, I, is injected from terminal T1 and the hot spot appears around T1 and T2, the potential, $V(r)$, measured between T1 and T2 ($T(r) > T_c$) becomes higher than those measured at T3 and T4 ($T(r) < T_c$), where the region is in an equipotential region as seen

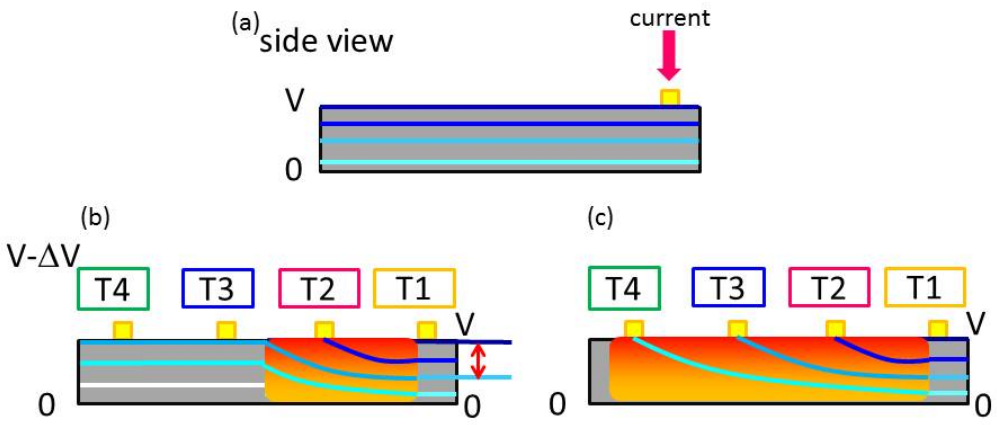

Fig. 34 The side view of the mesa device when (a) the entire mesa temperature is lower than T_c, (b) the hot-spot ($T(r) > T_c$) exists and (c)the entire mesa temperature is above T_c.

in Fig. 34(b). As we have seen before, the hot-spot size grows with increasing the current, I, or the bath temperature, T_b, and eventually $T(r)$ of the entire area of the mesa exceeds T_c as sketched in Fig. 34(c). In this case, the measured $V(r)$ must decrease as the distance from the current injection point is increased. Therefore, as seen in Figs. 33(a) and 33(b), ΔV becomes larger with increasing I and T_b since the hot-spot size grows. Moreover, we can understand that the reason of the sudden jump of ΔV(T3-T4) at $T_b(= 75\ \mathrm{K}) \simeq T_c$ is due to a growth of the normal conducting region.

In order to check the ac-Josephson relation, we have measured both the local electrical potential, $V(r)$, and the frequency, f, of the THz emission by the FT-IR at the same time. For this purpose, we made another mesa, sample #B, which has the dimensions of 81 μm in width, 400 μm in length and 2.6 μm in thickness. It has two electrode terminals denoted U and D attached which are separated by 300 μm, with two ground terminals (see the inset in Fig. 35(a)). Before the ac-Josephson effect measurements, we show the IVC measured by the two-probe technique and the emission intensity detected by the Si-bolometer at T_b=20 K in Figs. 35(a) and 35(b), respectively. Panels from(1) to (9) in Fig. 35(c) display the images of the temperature distribution of the mesa at T_b=20 K with the color code given as the right hand side in Fig. 35(c). Panel numbers (1) to (9) are in one-to-one correspondence with those given on the IVC in Fig. 35 (a). In this measurement, the current was always injected from terminal U and the hot spot appears there. It is clearly seen that the temperature at the hot

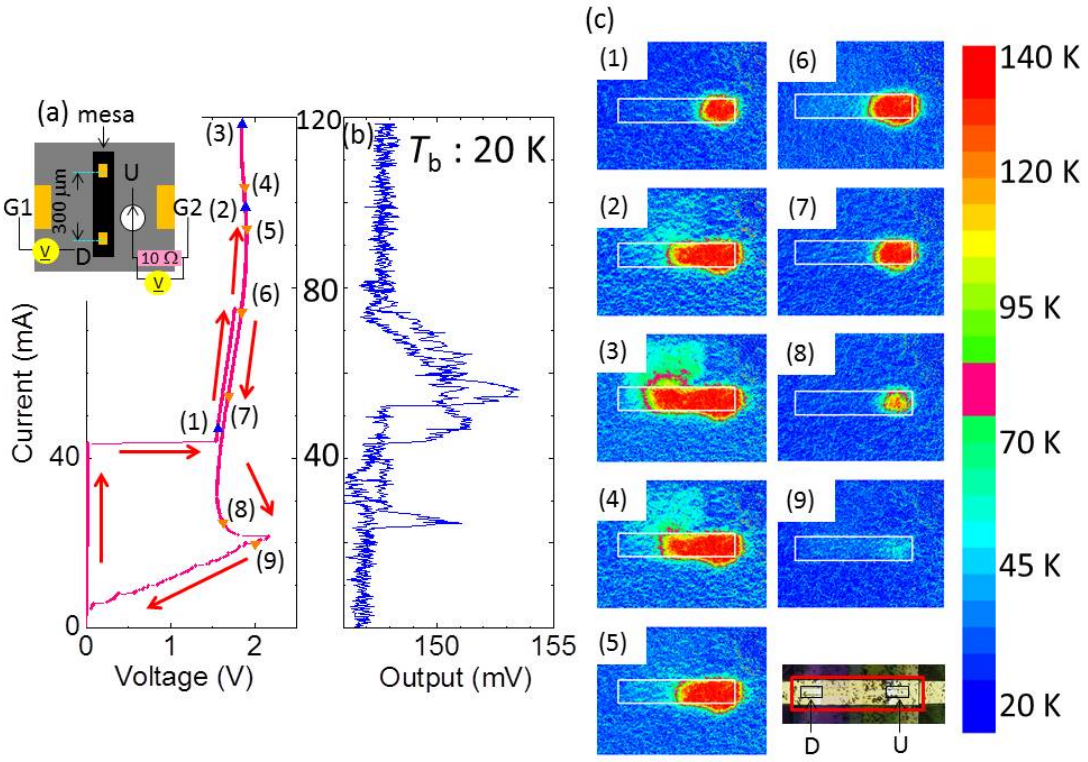

Fig. 35 (a) and (b) present the IVC measured by the two-probe technique and the emission intensity detected by the Si-bolometer as a function of the current, respectively. The current is always injected from the upper side of mesa device as shown in the inset of Fig. 35(a). (c) The images of the temperature distribution. The hot spot appears at the current injection point where the temperature is much higher than T_c.

spot is much higher than T_c. It even reaches $\sim$ 140 K.

Next, the local electrical potential distribution and the emission frequency by FT-IR spectrometer were measured simultaneously at T_b=45 K. The current was always fed in at terminal U (hot spot) and the voltages were measured at terminal U (hot spot) by the two-probe technique and at terminal D (superconductor) by the four-probe technique as shown in the equivalent electric circuit in the inset of Fig. 35(a). Figure 36(a) displays the IVC of the mesa measured by the four-probe technique (black) at D (superconductor) and by the two-probe technique before (purple) and after (gray) subtracting the contribution from the contact resistance at U (hot spot). As clearly seen in Fig. 36(a), the difference of the voltage between D (superconducting) and U (hot-spot) increases with increasing bias current, I. The same tendency was also seen in sample #A as described previously.

Figure 36(b) shows the emission frequency, f, measured by FT-IR spectrometer as a function of V measured by the two-probe technique after correction for the contact resistance (red

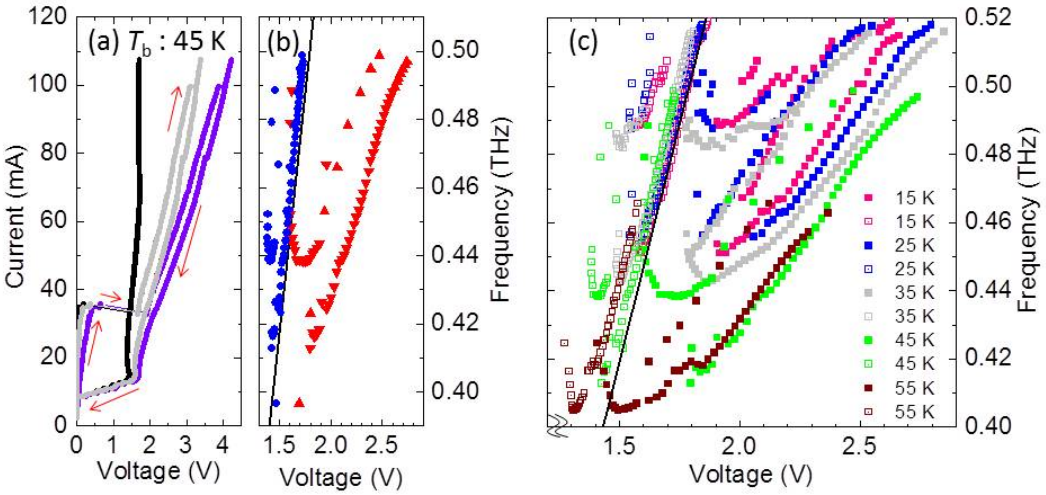

Fig. 36 (a) The IVCs of sample #B at 45 K obtained by the four-probe technique at the superconducting region (black) and by the two-probe technique at the heated region before (purple) and after (gray) correction for the contact resistance. (b) The emission frequency, f, as a function of the measured voltage, V, by the two-probe technique after correction for the contact resistance (red triangles) and the four-probe technique at the superconducting region (blue circles). We have made the same measurements as in Fig. 36(a) and 36(b) at several bath temperatures. These results are plotted in (c).

triangles) at U (hot spot) and by the four-probe technique (blue circles) at D (superconductor) at $T_{\rm b}$= 45 K. The black straight line in Fig. 36(b) shows the best fit to the ac-Josephson relation with the total number of intrinsic Josephson layers N=1732 layers. We can clearly see that the emission frequency follows the ac-Josephson relation within experimental error when the voltage was measured at D (superconductor) by the four-probe technique. Since the measured thickness of the mesa is 2.6 μm, which corresponds to 1742 layers (= 2.6 $\times$ 667(layers/1 μm)), this N value is in excellent agreement with the experimental value within an error of $\pm$0.6 % . In contrast, when V is measured by the two-probe technique at U (hot spot) even after correction for the contact resistance, the measured frequency, f, deviates significantly from the ac-Josephson relation. Such a tendencey was also seen in the previous work by Benseman *et al.* [45]. We added here similar data measured every 10 K between 15 K and 55 K as shown in Fig. 36(c) [51].

Concerning the mesa we used for our measurement and the one used by Benseman *et al.* [45], it is known that both of them have rather high residual resistances at the current injection

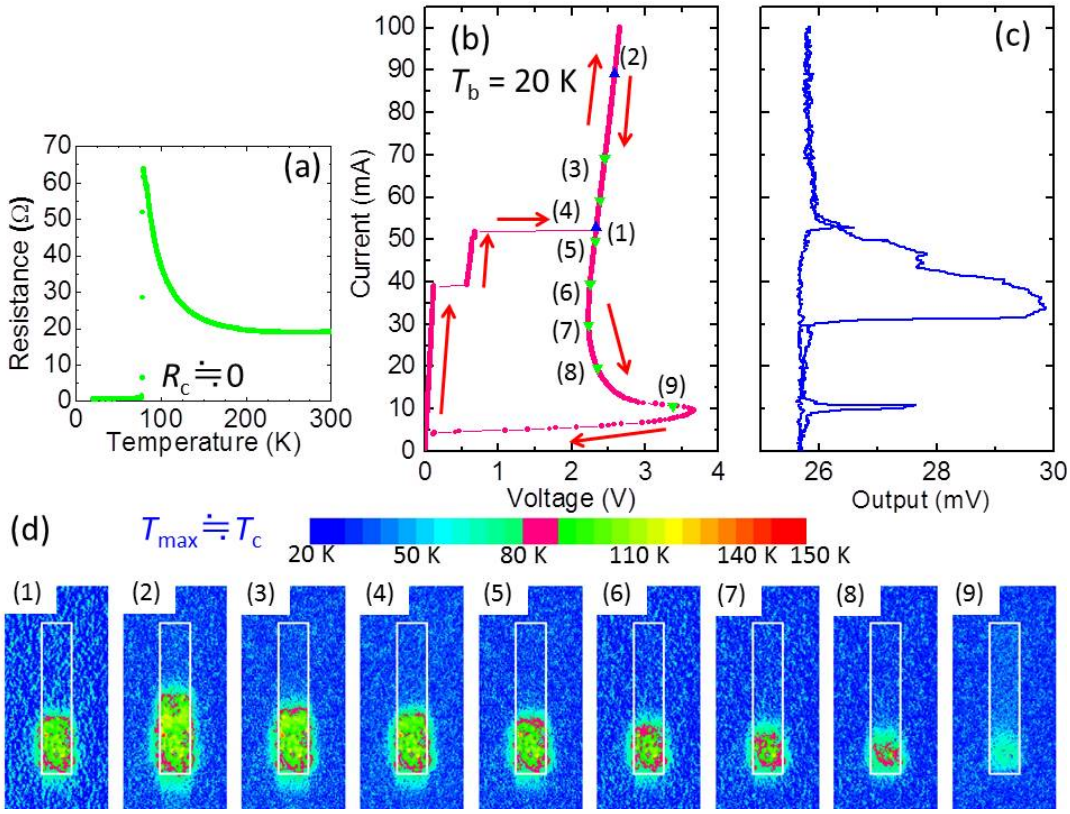

Fig. 37 (a) The temperature dependence of the c-axis resistance of sample #C. The contact resistance is almost zero which is much lower than that of samples #A and #B. (b)and (c) are respectively the IVC measured by the two-probe technique and the emission power detected the by hot-electron bolometer as a function of the biased current, I. (c) The panels from (1) to (9) are the $T(r)$ images of sample #C consisting to the IVC points in Fig. 37(b). The local temperature, $T(r)$, at the hot spot is as high as T_c.

point, so that it is expected that both $T(r)$s at those hot spots were much higher than T_c. We can ask an interesting question how the situation differs from the mesa which has less Joule heating. To answer this question, we made another mesa device with less Joule heating which is sample #C. This mesa sample #C has nearly the same dimensions as for samples #A and #B (78 μm x 400 μm x 3.0 μm), and has the same electrode terminals as has sample #B. In Fig. 37(a), the temperature dependence of the c-axis resistance is presented. As seen in Fig. 37(a), the contact resistance of sample #C is just about 3 Ω (including the wiring resistance which is as high as this value) which is much smaller than those of samples #A and #B.

Figures 37(b) and 37(c) are the IVC measured by the two-probe method and the emission intensity measured by the hot-electron bolometer at T_b=20 K, respectively. In this case, the current, I, is always injected from the lower side of the mesa device. The $T(r)$ images of sample #C are shown in the panels from (1) to (9) of Fig. 37(d), which were taken at the

various current values indicated in Fig. 37(b). As seen in the $T(r)$ images shown in Fig. 37(d), a hot spot emerges at the lower end of sample #C. It is noted that the maximum temperature of the hot spot observed in Fig. 37(d), does not greatly exceed T_c and is much lower than the maximum hot-spot temperatures observed in samples #A and #B. They are just above T_c but close to it. In addition, it is interesting to note that the hot-spot position is irrelevant to the location of the current, I, injection point. This means that the hot spot always forms at the lower end of the mesa, independent of which the electrical terminal, upper or lower, is used. Therefore, $T(r)$ distributions do not significantly differ from those shown in Fig. 37(d) even though the current is fed into the upper terminal.

Next, we show the relation between the electrical potential distribution, $V(r)$, and the radiation frequency, f. Figures 38(a) and 38(b) represent the IVCs measured using the electrode terminals located at the hot-spot region by the two-probe method and using the electrode terminal located at the superconducting region by the four-probe method, respectively, in 10 K steps from 10 K and 60 K. In this experiment, the current, I, is always injected from the lower end of sample #C. The black and orange solid rectangles in the insets of Figs. 38(a) and 38(b) respectively, indicate the electrode positions for the voltage, V, measurements. Therefore, it is obvious that the current injection point and the V measurement points are the same location at the central position of the hot spot as shown in the inset of Fig. 38(a). Figure 38(c) displays the difference in V between the $V(r)$ measured at the heated region and at the superconducting region, $\Delta V = V_{2\mathrm{probe}} - V_{4\mathrm{probe}}$, as a function of I from T_b=10 to 60 K in 10 K steps. Amazingly, the ΔV below $T_b \leqq 40$ K, agrees within less than 1 % of the total V and not depend on T_b, as seen in Fig. 38(c). We attributed such a small ΔV of sample #C to the smallness of the increase of $T(r)$ compared to that of samples #A and #B. On the other hand, ΔV suddenly jumps up above T_b= 50 K. This is because the change of the hot-spot behavior from a sharply well defined hot spot to a blurred hot spot, due to the increase in T_b. However, the tendency of the ΔV increase is similar to that of samples #A and #B.

Here, we would like to point out one experimental defect that is seen in the low current region in Fig. 38(c), *i.e.*, there is a little peak structure in ΔV. Although the origin of this is not well understood, we postulate that it may come from the contact resistance of the electrode, and that it should not affect our conclusions as described above. Figure 38(d) shows a figure plotting the emission frequency, f, as a function of the measured voltage, V. Here, we note that V measured at the heated region (hot-spot region expressed by the filled symbols) and the superconducting region (expressed by the open circles) is taken as the abscissa in Fig. 38(d) at several bath temperatures, although the contact resistance was corrected in the case of the data obtained by the two probe technique. As seen in Fig. 38(d), the data plotted are very similar and are indistinguishable. The color scale of the data points on the IVCs in Figs. 38(a) and 38(b) represents the emission power measured by the FT-IR spectrometer at a 45

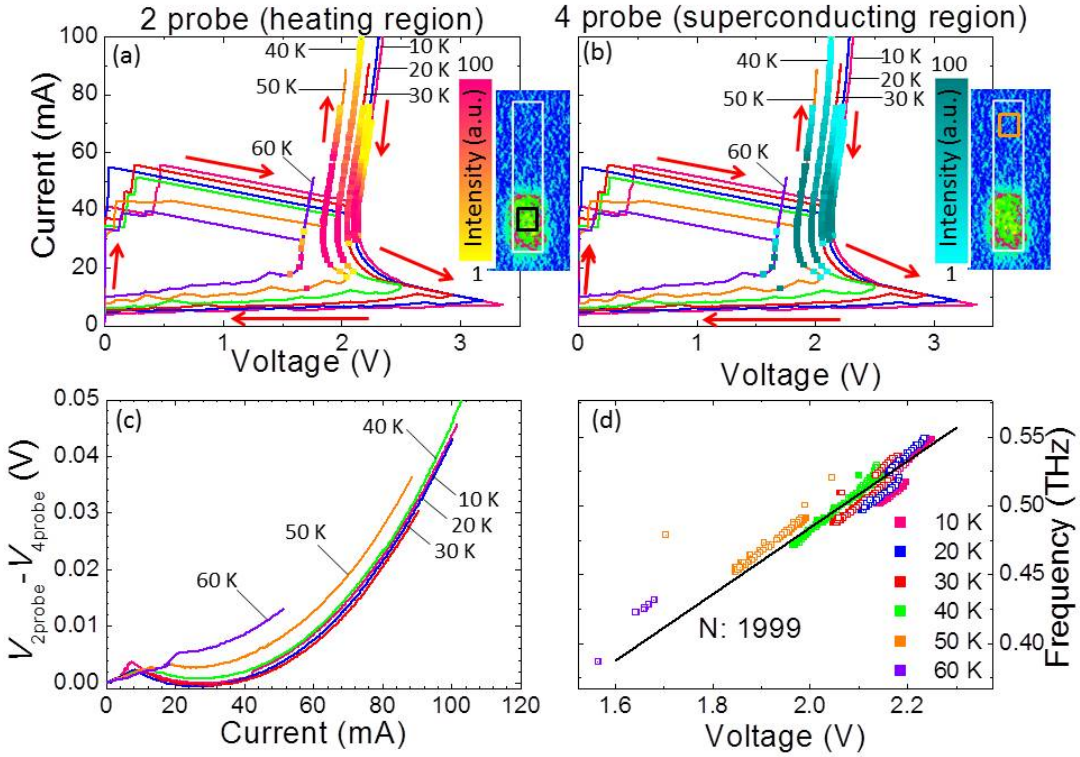

Fig. 38 (a) and (b) are the IVCs measured by the two-probe technique after correction for the contact resistance (heating region) and the four-probe technique (superconducting region) at 10 K to 60 K. (c) The difference in the voltages $\Delta V = V_{2\text{probe}} - V_{4\text{probe}}$ between that measured by the two-probe technique (heating region) and by the four-probe technique (superconducting region) as a function of the current, I. (d) The emission frequency frequency, f, as a function of the measured voltage, V, by the two-probe technique (filled symbols) and by the four-probe technique (open circles).

degree tilt from the c-axis of the sample. As seen in Figs. 38(a) and 38(b), the THz radiation can be observed over a wide bias-current region. The straight line in Fig. 38(d) indicates that the ac-Josephson relation works for N=1999, which is consistent with the N of sample #C (N=2001=3.0 μm x 667 layers/μm). The results shown in Fig. 38 tell us that the essential mechanism of the THz emission is the ac-Josephson effect. Moreover, whenever the mesa is not extensively over heated, the voltage as a function of the THz radiation frequency correctly obeys the ac-Josephson effect, even when coexisting with a hot spot.

9.3 Conclusion

In order to check and verify whether or not the ac-Josephson relation is valid in a rectangular mesa device in the hot-spot state, we have studied the emission frequency, f, the local

temperature distribution, $T(r)$, and the local electrical potential distribution, $V(r)$, simultaneously using three different mesas (#A, #B and #C) prepared separately. As a result, they have different characteristic behaviors with different amounts of Joule heating effect. Two (#A and #B) have large Joule heating due to large contact resistances at the electrodes, whereas the third one (#C) has less Joule heating due to a smaller contact resistance at the electrode. The emission spectra of them have been measured by the FTIR spectrometer. The local temperature distribution, $T(r)$, has been measured by the SiC photoluminescence technique as before, and the local electrical potential distribution, $V(r)$, has been measured by the multi-terminal four-probe technique along the long length of the mesa device. When the local voltage was measured at the heated region where $T(r) > T_c$ due to the hot-spot formation by a two probe-technique, the ac-Josephson relation nominally appears to have been strongly violated. However, when the local voltage, $V(r)$, was measured at the superconducting region by the four-probe technique, it is in good agreement with the ac-Josephson relation within the experimental error of 0.1 %. This behavior is clearly found in the mesas with the larger contact resistances and the larger Joule heating. On the contrary to this, in the case of the mesa with the lower contact resistance having less Joule heating(sample #C), both local voltages measured at the Joule heating region by the two-probe technique and these measured at the superconducting region by the four-probe technique give good agreement with the ac-Josephson relation within experimental error of 6 %.

In summary, we conclude here that if the mesa does not have a hot spot or if the heating effect is not strong enough to make $T(r) >> T_c$, the ac-Josephson relation works well, no matter where the local voltage was measured. However, when the mesa has significant Joule heat due to the contact resistance, for instance the local electrical potential, $V(r)$ has a largely inhomogeneous distribution along the long length of the mesa, and as a result $T(r) >> T_c$. In this case, only the local voltage obtained at the superconducting region gives the correct value that obeys the ac-Josephson effect. Therefore, it is confirmed that the ac-Josephson effect is the most primary source for the THz radiation, and it works as the origin of the THz radiation even though the mesa itself often has a temperature inhomogeneity, where the mesa temperature, $T(r)$, locally well exceeds T_c. It should be mentioned that the THz emission phenomenon can still survive even in such a chaotic temperature inhomogeneous state due to the hot-spot formation.

Part V

Summary

During my three years Ph.D. course, I have studied the Joule heating effect of the THz mesa device made of high-T_c superconducting $Bi_2Sr_2CaCu_2O_{8+\delta}$ intrinsic Josephson junctions on the THz emission phenomena. In order to understand the Joule heating effect as previously suggested by the LTSLM [34, 35], we recognized that the local temperature measurement is essentially important. Therefore, we have explored a new method to measure the local temperature distribution, $T(r)$, by using the temperature-dependent intensity of the photoluminescence emitted from the SiC micro-powders coated on the surface of the mesa device while it is in operation. The THz radiation intensity and frequency were also measured simultaneously. After several test runs, it was found that the strong temperature dependent PL emission is very reliable and reproducible with a spatial resolution of a few micrometers and the temperature resolution better than a few Kelvin. This was the standing point of my study.

The experimental results obtained by this method are summarized as follows:

When the dc current is increased above a critical value of I_c, at low temperature below $T_b \simeq 50$ K, a hot spot is created in the mesa, where superconductivity is destroyed because $T(r) \geq T_c$. We found many very surprising behaviors of the THz emitting mesa, although the hot spot is created and as a result the temperature of the mesa device becomes chaotic and very inhomogeneous. The formation of the hot spot means that the mesa has a normal conducting part in the rest of the superconducting part. The amazing phenomenon is that the THz emission survives even though the hot spot were created in the mesa. The radiation continues until the hot spot covers the whole region of the mesa. This suggests that the THz emission is a very tenacious phenomenon and can be generated as long as the mesa is even partially superconducting.

It seems that the position of the hot spot in the rectangular mesa affects the intensity of the THz emission but the frequency is almost unchanged. Although the reason for this peculiar behavior of the hot spot can not be well understood, the hot spot located at the middle part of the mesa seems to be most effectively suppressed. The THz radiation intensity appears to be the strongest while the hot-spot location lies at the edge region. From these experimental results on the relation between hot spot and the THz emission phenomena, the hot-spot formation severely deteriorates THz emission phenomenon so that it must be avoided as much as possible or it must be put aside from the center of the rectangular mesa. It may be the best for strong THz radiation to eliminate hot-spot formation in the mesa.

We have also learned that the THz radiation intensity can also be controlled by manipulating

the position of the hot spot, for example, by the focused laser beam. Roughly speaking from this experiment, the emission power can be increased at least a few times by optimizing the hot-spot position. Although the manipulation of the hot-spot position can improve the intensity a few times, the formation of the hot spot is not necessarily required to have THz radiation, especially the very strong THz radiation in the "retrap", on low current region, where there is no longer any hot spot in the mesa. This clear experimental finding is another very important piece of evidence in our study of the role of the hot spot, that the THz emission intensity is not enhanced but is deteriorated by its presence. Therefore, we disagree with the claim of Wang *et al.* [34, 35] in previous works, that the hot spot is necessary to have stronger THz radiation. Furthermore, the intimate correlation between the hot-spot size and the standing wave forming in the rest of the rectangular mesa area was not observed in our measurement at all. Such a wavy feature observed by Wang *et al.* may not be the standing of waves of the THz emission but may be something else.

It is confirmed that the ac-Josephson relation is valid even though the hot spot is formed. In this case, the voltage has to be measured at the place where there is no hot spot. This implies a very interesting idea for the design of the THz emitters: that it may be possible to separate the roles of a mesa device into two: one may be the source of the THz radiation and the others may be the resonator to enhance the intensity of radiation from the source. Such a division of the roles may lead to intense THz emitting devices in the future.

As described above, we understand the role of the hot spot and the effects of it on the THz radiation fairly well from the experimental results performed during my Ph.D. study. It is clear that enormous heat generation gives negative effects on the THz radiation in most cases, as expected from common sense. However, the recent line-width measurement showed an unusual behavior that it becomes narrower at higher temperatures, contradicting common sense. This might suggest some positive temperature effect, because the narrower line width would mean better coherence effect, as found by Li *et al.* [53].

In addition, it is still not clear how much emission power can be extracted from the mesa. This question has to be answered by the future study in this fascinating THz emission phenomenon in high-T_c intrinsic Josephson junction system made of single crystal $Bi_2Sr_2CaCu_2O_{8+\delta}$.

References

[1] Hua Zhong, Albert Redo-Sanchez and X. -C. Zhang, OPTICS EXPRESS **14**, 9130-9141 (2006).

[2] B. M. Fischer, M. Walther and P. Uhd Jepsen, Phys. Med. Biol. **47**, 3807 (2002).

[3] for example, M. Tonouchi, Nat. Photon. **1**, 97 (2007).

[4] J. Faist *et al.*, Science **264**, 553 (1994).

[5] L. Esaki, IEEE Trans. on Electron Devices **23**, 644 (1976).

[6] M. Asada and S. Suzuki, J. Infrared Milli Terahertz waves **37**, 1185-1198 (2016).

[7] L. Ozyuzer *et al.*, Science **318**, 1291 (2007).

[8] B. D. Josephson, Phys. Lett. **1**, 251 (1962).

[9] P. W. Anderson and J. M. Rowell, Phys. Rev. Lett. **10**, 230 (1963).

[10] R. Feynman, R. Leighton and M. Sands, "The Feynman Lecture in Physics", Vol. III, 21-14 (2006).

[11] M. D. Fiske, Rev. Mod. Phys. **36**, 221 (1964).

[12] http://physics.nist.gov/cgi-bin/cuu/Value?e

[13] S. Shapiro, Phys. Rev. Let. **11**, 80 (1963).

[14] K. Yanson *et al.*, JETP **47**, 2091(1964), also Soviet Phys. JETP **20**, 1404 (1965).

[15] A. K. Jain *et al.*, Phys. Rep. **109**, 309 (1984).

[16] P. Barbara *et al.*, Phys. Rev. Lett. **82**, 1963 (1999).

[17] R. Kleiner *et al.*, Phys. Rev. Lett. **68**, 2394 (1992).

[18] W. Anderson, Phys. Rev. **110**, 827 (1958).

[19] Y. Matsuda *et al*, Phys. Rev. Lett. **75**, 4512 (1995).

[20] Ophelia K. C. Tsui *et al.*, Phys. Rev. Lett. **73**, 724 (1994).

[21] T. Tachiki, T. Koyama, and S. Takahashi, Phys. Rev. B **50**, 7065 (1994).

[22] T. Tachiki, T. Koyama, and S. Takahashi, Physics C **263**, 1-11 (1996).

[23] T. Tachiki, S. Takahashi and K. Kadowaki, Physics C **282-287**, 2421 (1997).

[24] K. Kadowaki, *et al.*, Physica **239**, 123 (1997).

[25] K. Kadowaki, *et al.*, Phys. Rev. B **56**, 5617 (1997).

[26] K. Kadowaki, *et al.*, Europhys. Lett. **42**, 203 (1998).

[27] I. Kakeya *et al*, Phys. Rev. B **57**, 3108 (1998).

[28] M. Tsujimoto, *et al.*, Phys. Rev. Lett. **105**, 037005 (2010).

[29] T. M. Benseman, *et al.*, Appl. Phys. Lett. **103**, 022602 (2013).

[30] S. Sekimoto *et al.*, Appl. Phys. Lett. **103**, 182601 (2013).

[31] T. Kashiwagi *et al.*, Appl. Phys. Lett. **106**, 092601 (2015).

[32] H. Minami *et al.* J. Phys.: Condens. Matter **28**, 025701 (2016).

[33] T. Kashiwagi, *et al.*, Appl. Phys. Lett. **107**, 082601 (2015).
[34] H. B. Wang, *et al.*, Phys. Rev. Lett. **102**, 017006 (2009).
[35] H. B. Wang, *et al.*, Phys. Rev. Lett. **105**, 057002 (2010).
[36] S. Guénon *et al*, Phys. Rev. B **82**, 214506 (2010).
[37] A. Yurgens, Phys. Rev. B **83**, 184501 (2011).
[38] B. Gross *et al.*, Phys. Rev. B **86**, 094524 (2012).
[39] S. Niratisairak *et al.*, Physica C **468**, 442-446 (2008).
[40] S. Niratisairak *et al.*, Physica C **471**, 222-225 (2011).
[41] R. A. Klemm and K. Kadowaki, J. Phys.: Condens. Matter **22**, 375701 (2010).
[42] X. Zhou *et al.*, Appl. Phys. Lett. **107**, 122602 (2015).
[43] M. Tsujimoto *et al.*, Phys. Rev. Appl. **2**, 044016 (2014).
[44] T. Kitamura *et al.*, Appl. Phys. Lett. **105**, 202603 (2014).
[45] T. M. Benseman, *et al.*, Supercond. Sci. Technol. **26**, 085016 (2013).
[46] M. Tsujimoto, *et al.*, Phys. Rev. Lett. **108**, 107006 (2012).
[47] H. Minami, *et al.*, Phys. Rev. B **89**, 054503 (2014).
[48] C. Watanabe, *et al.*, J. Phys.: Condens. Matter **26**, 172201 (2014).
[49] T. M. Benseman, *et al.*, J. Appl. Phys. **113**, 133902 (2013).
[50] C. Watanabe, *et al.*, Appl. Phys. Lett. **106**, 042603 (2015).
[51] C. Watanabe *et al.*, Supercond. Sci. Technol. **29**, 065022 (2016).
[52] T. Mochiku, K. Hirata, and K. Kadowaki, Physica C **282-287**, 475-476 (1997).
[53] M. Li *et al.*, Phys. Rev. B **86**, 060505 (2012).

Research Achievement

Publication to the scientific journals with the first author

1. C. Watanabe, H. Minami, T. Yamamoto, T. Kashiwagi, R. A. Klemm and K. Kadowaki, J. Phys.: Condens. Matter **26**, 172201 (2014).
2. C. Watanabe, H. Minami, T. Kitamura, K. Asanuma, K. Nakade, T. Yasui, Y. Saiwai, Y. Shibano, T. Yamamoto, T. Kashiwagi, Richard A. Klemm, and K. Kadowaki , Appl. Phys. Lett. **106**, 042603 (2015).
3. Chiharu Watanabe, Hidetoshi Minami, Takeo Kitamura, Yoshihiko Saiwai, Yuki Shibano, Takuya Katsuragawa, Hiroyuki Kubo, Kazuki Sakamoto, Takanari Kashiwagi, Richard A Klemm and Kazuo Kadowaki, Supercond. Sci. Technol. **29**, 065022 (2016).

Publication to the scientific journals with the co-author

1. Daniel P Cerkoney, Candy Reid, Constance M Doty, Ashley Gramajo, Tyler D Campbell, Manuel A Morales, Kaveh Delfanazari, Manabu Tsujimoto, Takanari Kashiwagi, Takashi Yamamoto, Chiharu Watanabe, Hidetoshi Minami, Kazuo Kadowaki, and Richard A Klemm, Journal of Physics: Condensed Matter **29**, 015601 (2016).
2. T Kashiwagi, T Yamamoto, H Minami, M Tsujimoto, R Yoshizaki, K Delfanazari, T Kitamura, C Watanabe, K Nakade, T Yasui, K Asanuma, Y Saiwai, Y Shibano, T Enomoto, H Kubo, K Sakamoto, T Katsuragawa, B Markovic, J Mirkovic, RA Klemm, K Kadowaki, Phys. Rev. Appl. **4**, 054018 (2015).
3. Takanari Kashiwagi, Kazuki Sakamoto, Hiroyuki Kubo, Yuuki Shibano, Takuma Enomoto, Takeo Kitamura, Kentaro Asanuma, Takaki Yasui, Chiharu Watanabe, Kurama Nakade, Yoshihiko Saiwai, Takuya Katsuragawa, Manabu Tsujimoto, Ryozo Yoshizaki, Takashi Yamamoto, Hidetoshi Minami, Richard A Klemm, Kazuo Kadowaki, Appl. Phys. Lett. **107**, 082601 (2015).
4. TM Benseman, AE Koshelev, V Vlasko-Vlasov, Y Hao, W-K Kwok, U Welp, C Keiser, B Gross, M Lange, D K le, R Kleiner, H Minami, C Watanabe, K Kadowaki, Phys. Rev. Appl. **3**, 044017 (2015).
5. Takanari Kashiwagi, Takashi Yamamoto, Takeo Kitamura, Kentaro Asanuma, Chiharu Watanabe, Kurama Nakade, Takaki Yasui, Yoshihiko Saiwai, Yuuki Shibano, Hiroyuki Kubo, Kazuki Sakamoto, Takuya Katsuragawa , Manabu Tsujimoto, Kaveh Delfanazari, Ryozo Yoshizaki, Hidetoshi Minami, Richard A. Klemm, and Kazuo Kadowaki, Appl. Phys. Lett. **106**, 092601 (2015).
6. T. Kitamura, T. Kashiwagi, T. Yamamoto, M. Tsujimoto, C. Watanabe, K. Ishida, S. Sekimoto, K. Asanuma, T. Yasui, K. Nakade, Y. Shibano, Y. Saiwai, H. Minami, R. A.

Klemm, and K. Kadowaki, Appl. Phys. Lett. **105**, 202603 (2014).

7. T. Kashiwagi, K. Nakade, Y. Saiwai, H. Minami, T. Kitamura, C. Watanabe, K. Ishida, S. Sekimoto, K. Asanuma, T. Yasui, Y. Shibano, M. Tsujimoto, T. Yamamoto, B. Markovic, J. Mirkovic, R. A. Klemm and K. Kadowaki, Appl. Phys. Lett. **104**, 082603 (2014).
8. H. Minami, C. Watanabe, K. Sato, S. Sekimoto, T. Yamamoto, T. Kashiwagi, R. A. Klemm and K. Kadowaki, Phys. Rev. B **89**, 054503 (2014).
9. T. Kashiwagi, K. Nakade, B. Markovic, Y. Saiwai, H. Minami, T. Kitamura, C. Watanabe, K. Ishida, S. Sekimoto, K. Asanuma, T. Yasui, Y. Shibano, M. Tsujimoto, T. Yamamoto, J. Mirkovic, and K. Kadowaki, Appl. Phys. Lett. **104**, 022601 (2014).
10. K. Delfanazari, H. Asai, M. Tsujimoto, T. Kashiwagi, T. Kitamura, K. Ishida, C. Watanabe, S. Sekimoto, T. Yamamoto, H. Minami, M. Tachiki, R. A. Klemm, T. Hattori and K. Kadowaki, J Infrared Milli Terahertz Waves **35**, 131-146 (2014).
11. Takeo Kitamura, Takanari Kashiwagi, Manabu Tsujimoto, Kaveh Delfanazari, Masashi Sawamura, Kazuya Ishida, Shunsuke Sekimoto, Chiharu Watanabe, Takashi Yamamoto, Hidetoshi Minami, Masashi Tachiki, Kazuo Kadowaki, Physica C: Superconductivity **494**, 117-120 (2013).
12. S. Sekimoto, C. Watanabe, H. Minami, T. Yamamoto, T. Kashiwagi, R. A. Klemm and K. Kadowaki, Continuous 30 μW terahertz source by a high-T_c superconductor mesa structure, Appl. Phys. Lett. **103**, 182601 (2013).
13. Kazuo Kadowaki, Manabu Tsujimoto, Kaveh Delfanazari, Takeo Kitamura, Masashi Sawamura, Hidehiro Asai, Takashi Yamamoto, Kazuya Ishida, Chiharu Watanabe, Shunsuke Sekimoto, Kurama Nakade, Takaki Yasui, Kentaro Asanuma, Takanari Kashiwagi, Hidetoshi Minami, Masashi Tachiki, Toshiaki Hattori, Richard A Klemm, Physica C: Superconductivity **491**, 2-6 (2013).
14. T. M. Benseman, A. E. Koshelev, W.-K. Kwok, U. Welp, V. K. Vlasko-Vlasov, K. Kadowaki, H. Minami and C. Watanabe, J. Appl. Phys. **113**, 133902 (2013).
15. K. Delfanazari, H. Asai, T. Kashiwagi, T. Kitamura, T. Yamamoto, M. Sawamura, K. Ishida. C. Watanabe, S. Sekimoto, H. Minami, M. Tachiki, R. A. Klemm, T. Hattori and K. Kadowkai, Optics Express **21**, 2171-2184 (2013).

Acknowledgement

I would like to express my special appreciation and sincere thanks to Professor Kazuo Kadowaki whose detailed comments and suggestion are always helpful. Furthermore, Prof. Kadowaki always supported and encouraged me with his patience and gave me strong motivation and direction suggesting the optimum path and leading to the best conditions with immense knowledge when I lost my way in research as well as in my life. I also would like to express my sincere gratitude to Prof. Ryozo Yoshizaki, Dr. Manabu Tsujimoto, Prof. Itsuhiro Kakeya and Prof. Richard Klemm for their fruitful discussions and advice. Discussions with Prof. Dr. R. Kleiner, Drs. H. B. Wang, W.-K. Kwok, U. Welp, and T. M. Benseman have also been stimulating and illuminating. I am indebted to Mr Mitsuhiro Muroi, a technical staff member of their department for his excellent programming to help data analysis. I received generous and kind support from Dr. Hidetoshi Minami and Dr. Takanari Kashiwagi. Dr. Takeo Kitamura, Mr. Syunsuke Sekimoto, Mr. Kazuya Ishida and Dr. Takashi Yamamoto have been greatly tolerant and supportive. I appreciate the theoretical feedback offered by Dr. Hidehiro Asai and Dr. Shiro Kawabata. I would also like to thank all the members in Kadowaki-Kashiwagi, Minami and Tsujimoto laboratory giving me many new insights for writing this thesis. Thank you very much for my all friends, especially Aohang Wang, who worked and enjoyed with me during my three years of graduate school time.

Finally, a special thanks to my family, especially my delightful mother and flashy baby sister for their warm support and encouragement. I also would like to thank my grandmother and grand father in heaven.

This research was partly supported by the JSPS Fellowship for young scientists from the Japan Society for the promotion of Science (JSPS) (Grant-in-Aid Numbers 263097).